Applied Mathematics and Computation 440 (2023) 127642

Contents lists available at ScienceDirect

Applied Mathematics and Computation

journal homepage: www.elsevier.com/locate/amc

Extension of a Roe-type Riemann solver scheme to model non-hydrostatic pressure shallow flows

I. Echeverribar[a,b,*], P. Brufau[a], P. García-Navarro[a]

[a] I3A, University of Zaragoza, Zaragoza, Spain
[b] Hydronia Europe, S. L., Madrid, Spain

ARTICLE INFO

Article history:
Received 17 May 2022
Revised 14 October 2022
Accepted 15 October 2022
Available online 31 October 2022

Keywords:
Non hydrostatic pressure
Steady/unsteady
Implicit/explicit
Full-hyperbolic
Roe solver

ABSTRACT

The aim of this work is, first of all, to extend a finite volume numerical scheme, previously designed for hydrostatic Shallow Water (SWE) formulation, to Non Hydrostatic Pressure (NHP) depth averaged model . The second objective is focused on exploring two available options in the context of previous work in this field: Hyperbolic-Elliptic (HE-NHP) formulations solved with a Pressure-Correction technique (PCM) and Hyperbolic Relaxation formulations (HR-NHP). Thus, besides providing an extension of a robust and well-proved Roe-type scheme developed for hydrostatic SWE to solve NHP systems, the work assesses the use of first order numerical schemes in the kind of phenomena typically solved with higher order methods. In particular, the relative performance and differences of both NHP numerical models are explored and analysed in detail. The performance of the models is compared using a steady flow test case with *quasi*-analytical solution and another unsteady case with experimental data, in which frequencies are analysed in experimental and computational results. The results highlight the need to understand the behaviour of a parameter-dependent model when using it as a prediction tool, and the importance of a proper discretization of non-hydrostatic source terms to ensure stability. On the other hand, it is proved that the incorporation of a non-hydrostatic model to a shallow water Roe solver provides good results.

1. Introduction

The 3D incompressible Navier–Stokes Equations (NSE), or even the frictionless 3D Euler Equations, involve a complexity that has traditionally favored the existence of simple models for free surface analysis at the cost of losing the generality of the initial system. In particular, when dealing with complex bathymetry, the shallow water models have been frequently used. They are often applied when vertical variations are not relevant and the momentum equations can be depth-averaged, resulting in pressure distributions like the one seen in the momentum equation z in the absence of friction terms [1]:

$$\frac{p}{\rho} = g(h_s - z) + \int_z^{h_s} \left(\frac{\partial w}{\partial t} + u\frac{\partial w}{\partial x} + v\frac{\partial w}{\partial y} + w\frac{\partial w}{\partial z} \right) dz. \tag{1}$$

* Corresponding author at: I3A, University of Zaragoza, Zaragoza, Spain.
E-mail address: echeverribar@unizar.es (I. Echeverribar).

https://doi.org/10.1016/j.amc.2022.127642

where p stands for pressure, ρ is the density, g is the gravity acceleration, h_s is the water surface level, z is the vertical coordinate and u, v, w are the velocity components in the x, y, z directions respectively. These models can be used to solve the three flow velocity components in a 3D flow. There exists a variety of physical models that deal with free surface flows, some of them preserve vertical acceleration [2–4], while others assume a hydrostatic pressure vertical distribution [5,6].

Alternatively, a 3D free surface flow model can be reduced spatially through vertical integration and the application of bottom and free surface boundary conditions [7], leading to a two-dimensional (2D) model, in terms of the thickness h (water depth) and two components of the depth averaged velocity, where boundaries are no longer on the surface and the bottom but on the perimeter. All the models discussed in the present work are depth averaged.

In this context, the Saint–Venant system of equations is a depth averaged shallow water system of equations whose main hypothesis is that the vertical pressure distribution is hydrostatic. They are typically applied to situations in which vertical accelerations can be neglected in comparison to gravity terms in (1), hence leading to a hydrostatic vertical pressure distribution as:

$$\frac{p}{\rho} \approx g(h_s - z) \tag{2}$$

This approach is considered suitable for some geophysical flows such as rivers, mud slurries, lava flows and rainfall-runoff processes among others. However, the assumption of hydrostatic pressure and the fact that vertical accelerations are neglected, may provide inaccurate results when modelling dispersive phenomena, such as those occurring in wave propagation, or when dealing with vertical accelerations, i.e., flow over an obstacle.

The preservation of non-hydrostatic terms and vertical effects has been studied from different viewpoints in the context of depth averaged formulations. On the one hand, different approximations of the velocity integrals, some of them arising from the assumption of potential flow, can be used to derive dispersive terms that formulate the non-hydrostatic pressure [8] present in the integral of (1). Depending on the assumed hypothesis, these terms give rise to different models, such as the Boussinesq model, the Green–Naghdi model (that can be extended to the Serre–Green–Naghdi) or the Su–Gardner model, all of them called here Dispersive Shallow Water models (DSW) [9,10]. New high order derivatives appear and, depending on the hypotheses assumed during this process, the dispersive terms provide different behaviour to the model [8,9]. Additionally, this new high-order derivatives present a numerical challenge when solving. Recent works solve the system into two steps [11] or even improve the methodology by means of a relaxation of the system [12]. Some other works as Busto et al. [13], Bassi et al. [14] focus on the very-high order numerical scheme to solve the system. An alternative are the so-called Boussinesq models, that were first derived by Peregrine [15] for smooth bottoms and are not suitable to deal with strong bottom discontinuities, as seen in Nadiga et al. [9]. During decades, improvements in these models have been developed to solve their weak dispersion and to extend their validity to deeper water problems [16,17]. Although more accurate representation of phase and group celerities in waves has been achieved by these extensions, fluid motion is still not enough well described. Green–Naghdi (GN) models deal with irregular topography, however they are not able to reproduce wave breaking phenomena. As reported by Orgaz and Chanson [8], who solved the dam-break problem with different GN models, it all depends on the terms kept in the derivation process. Some works add an energy dissipating mechanism that mimics the breaking phenomenon; others derive the equations adding some terms neglected by the traditional system, giving rise to the Su–Gardner system, which is able to dissipate this energy when necessary, for instance, in wave breaking problems [8]. Recently, some models have arisen to provide more accurate definition of velocities and reproduce these phenomena that traditional DSW models are not able to solve [18]. However, these models are parameterized and need closure relations. Another alternative to preserve more vertical information is the use of multilayer systems, that can perform properly when simulating this phenomena [19,20].

Alternatively to DSW models, according to Bristeau et al. [21], pressure can be divided into a hydrostatic part, dependent on water depth, and a non-hydrostatic part, p_{nh}:

$$\frac{p}{\rho} = g(h_s - z) + \frac{p_{nh}}{\rho} \tag{3}$$

Models that follow this approach will be named non-hydrostatic pressure (NHP) models in the present work. In contrast to DSW models, NHP models introduce a new variable, p_{nh}, to gather all the dispersive terms that appear when solving the integral in (1). Thus, these models require a closure relation to complete the system. Several approaches can be applied in this case, being one of the most common the *Pressure Correction Method* (PCM) [22,23]. This method, also termed fractional time step procedure in the literature, consists in the resolution of the system with an iterative approach to find the p_{nh} value that guarantees the continuity equation. As initial guess $p_{nh} = 0$, and the system is solved as a hydrostatic model. This provides a hydrostatic velocity field that does not necessarily satisfy the incompressible flow continuity equation ($\nabla \cdot \mathbf{v} = 0$). Hence, enforcing this equation, the velocity field is modified through a pressure correction, p_{nh}. This methodology is widely extended combining different techniques. For the advective terms in the hydrostatic step, Yamazaki [24] used a finite difference explicit scheme, as well as Casulli [25,26], while siouene [27] applied a finite volume approach and Escalante [28] solved this part combining a MUSCL reconstruction operator with a PVM method. In spite of the different numerical techniques used for the hydrostatic part, all works use a correction step after the hydrostatic resolution, fixing the hydrostatic velocity field with p_{nh}.

The problem with this two-step methodology lies in the closure relation. To obtain p_{nh} it is necessary to solve an elliptic equation uncoupled from the rest of the hyperbolic system, that needs an implicit numerical scheme or an iterative method.

The development of implicit numerical methods has also evolved and has become more efficient [29–31]. However, it still entails an optimization challenge today, especially when the computation of these problems is geared towards parallelization to speed up simulations on large environmental problems. For this reason, some recent works have proposed alternatives to construct an evolution equation for p_{nh} that allows to solve the whole system in a coupled way [32]. This approach is based on the artificial compressibility (ACM) model [32,33], and provides a new hyperbolic equation for p_{nh}. However, the main drawback of the method is the incorporation of a parametric celerity [32], and its formulation based on a reference water depth, which could not be accurate enough when dealing with an irregular topography.

DSW and NHP models have been mainly applied to wave propagation on coastal phenomena, such as wave run-up and wave shoaling due to their capability of reproducing nearshore dynamics preserving both nonlinear and dispersive effects. Therefore, those models have been often solved by means of high order numerical schemes in order to reduce the numerical diffusion [13,14,28,32,34]. However, their application in other free surface hydraulic problems is less frequent due to their complexity and the computational cost associated to by the additional terms in the equations. This is one of the reasons why the work of Escalante with ACM models [32] is of great interest to the computational hydraulic community. The emergence of purely explicit schemes gives way to an opportunity for parallelization and high performance computing (HPC).

Realistic environmental problems involve complex geometries and huge domains with a large intrinsic computational load. The most widespread approach in this context is the hydrostatic SW system, especially for applications where the source terms play a dominant role. The correct form to solve hydrostatic SW systems with source terms to produce robust schemes has been a fruitful matter of research in the last decades [35–39].

The aim of this work is, first of all, to extend a finite volume numerical scheme previously designed for hydrostatic SW [40], that has already been applied in large domains with great success [35], to NHP models. The second objective is to explore the available options in the context of previous work. Thus, besides providing an extension of a robust and well-proved Roe-type scheme developed for hydrostatic SWE to solve NHP systems, the work assesses the use of first order numerical schemes to deal with the kind of phenomena typically solved with higher order methods. In particular, the performance and differences of two NHP models are explored and analysed: the classical PCM applied to a hyperbolic-elliptic NHP model (*HE-NHP*) and the hyperbolic relaxation presented by Escalante [32], referred as *HR-NHP*. The numerical details of a first order finite volume (FV) numerical scheme were previously developed [40–43] and demonstrated to be robust and efficient [35] specially in the presence of source terms.

In the present work, both models are applied to unsteady and steady states. To do the latter test, a *quasi*-analytical steady reference solution of Bristeau et al. [21] is used as reference solution of the HE-NHP system. Additionally, a new steady state solution for the HR-NHP system is provided and used to be compared with numerical results.

The outline of the paper is as follows: first the equations used in the 1D HE-NHP and HR-NHP models are presented, then the finite volume method used is described with focus on the Roe formulation adopted for the hyperbolic parts of both models. The propagation of a solitary wave is used as first test case to analyse the proper discretization of the non-hydrostatic source term in HR-NHP model and to perform a convergence analysis of all the models. The performance of the models is compared using a steady flow test case with exact solution and another unsteady case with experimental data, where frequencies are analysed in experimental and computational results through Fast Fourier Transport (FFT) analysis. Finally, discussion and conclusions are provided.

2. Governing equations

2.1. Derivation of a depth averaged non-hydrostatic pressure system

The incompressible, frictionless flow mass and momentum equations (Euler) in the (x, z) vertical plane, can be written as

$$\begin{cases} \dfrac{\partial u}{\partial x} + \dfrac{\partial w}{\partial z} = 0, & \text{(4a)} \\ \dfrac{\partial u}{\partial t} + u\dfrac{\partial u}{\partial x} + w\dfrac{\partial u}{\partial z} + \frac{1}{\rho}\dfrac{\partial p}{\partial x} = 0, & \text{(4b)} \\ \dfrac{\partial w}{\partial t} + u\dfrac{\partial w}{\partial x} + w\dfrac{\partial w}{\partial z} + \frac{1}{\rho}\dfrac{\partial p}{\partial z} = -g. & \text{(4c)} \end{cases}$$

and must be completed with free surface and bottom boundary conditions [21]. In order to develop a NHP model, the expression of (3) can be adopted, involving a new variable p_{nh}. By integrating in the water column, applying boundary conditions and substituting the total pressure, the system in the frictionless case yields

$$\begin{cases} \dfrac{\partial h}{\partial t} + \dfrac{\partial (h\bar{u})}{\partial x} = 0, & \text{(5a)} \\ \dfrac{\partial (h\bar{u})}{\partial t} + \dfrac{\partial}{\partial x}\left(\dfrac{(h\bar{u})^2}{h} + \dfrac{1}{2}gh^2 + \dfrac{1}{\rho}(h\bar{p}_{nh}) \right) = -(gh + \dfrac{2}{\rho}\bar{p}_{nh})\dfrac{\partial z_b}{\partial x}, & \text{(5b)} \\ \dfrac{\partial (h\bar{w})}{\partial t} + \dfrac{\partial}{\partial x}\left(\dfrac{(h\bar{u})(h\bar{w})}{h} \right) = \dfrac{2}{\rho}\bar{p}_{nh}. & \text{(5c)} \end{cases}$$

where h represents the water depth, $\bar{u}$ and $\bar{w}$ will stand for the depth averaged velocities, defined as

$$\bar{u} = \frac{1}{h}\int_{z_b}^{h_s} u dz \qquad \text{and} \qquad \bar{w} = \frac{1}{h}\int_{z_b}^{h_s} w dz, \tag{6}$$

$\bar{p}_{nh}$ is the depth averaged non-hydrostatic pressure, and z_b represents the bottom surface level. From now on, the depth averaged variables will be represented without the overbar for the sake of clarity. Also, as the density is assumed to be constant and equal to 1, this variable will not be included in the formulation.

System (5) needs an additional equation in order to solve the four variables. In the case of the HE-NHP model, the consideration of the original incompressibility condition is the additional equation, explained in Section 2.2. On the other hand, a hyperbolic relaxation of the system can be done to obtain an equation that represents the evolution of p_{nh}, leading to the HR-NHP model, as explained in Section 2.3.

2.2. HE-NHP: hyperbolic-elliptic non hydrostatic pressure model

The system is formed by the depth integrated mass conservation Eq. (5a) and two momentum equations in the x and z directions, (5b) and (5c). According to Bristeau et al. [21], another equation can be used that derives from the divergence free condition ($\nabla \cdot \mathbf{v} = 0$), commonly named Depth Integrated Incompressibility Condition (DIIC) [24,28]. When integrating the divergence-free condition between the bottom, z_b, and the water surface level, h_s, the equation yields

$$\frac{\partial}{\partial x}\int_{z_b}^{h_s} u dz - u(h_s)\frac{\partial h_s}{\partial x} + u(z_b)\frac{\partial z_b}{\partial x} + w(h_s) - w(z_b) = 0. \tag{7}$$

Assuming a constant profile for $u(z) = u$ and a linear profile for $w(z) = w(z_b) + \dfrac{w(h_s) - w(z_b)}{h} z$, the vertical averages are easy. Thus, applying the bottom boundary condition $w(z_b) = u(\partial z_b/\partial x)$:

$$\begin{cases} \frac{\partial h}{\partial t} + \frac{\partial (hu)}{\partial x} = 0, & \text{(8a)} \\ \frac{\partial (hu)}{\partial t} + \frac{\partial}{\partial x}\left(\frac{(hu)^2}{h} + \frac{1}{2}gh^2 + (hp_{nh})\right) = -(gh + 2p_{nh})\frac{\partial z_b}{\partial x}, & \text{(8b)} \\ \frac{\partial w}{\partial t} + u\frac{\partial w}{\partial x} = \frac{2p_{nh}}{h} & \text{(8c)} \\ h\frac{\partial (hu)}{\partial x} + 2hw - hu\frac{\partial (h+2z_b)}{\partial x} = 0. & \text{(8d)} \end{cases}$$

Note that, unlike the other three, (8d) is not a time evolution equation but it presents an elliptic term which is the reason to give the name of hyperbolic-elliptic (HE-NHP) system requiring an implicit step to solve it. Additionally, the z-momentum Eq. (5c) can be rewritten as a transport equation for the vertical velocity component as (8c).

Eqs. (8a) and (8b) can be grouped in a system of conservation laws where the advective terms in the two first equations are the same as those of the Saint–Venant equations.:

$$\begin{cases} \frac{\partial \mathbf{U}}{\partial t} + \frac{\partial \mathbf{F}(\mathbf{U})}{\partial x} = \mathbf{S}_b(\mathbf{U}) + \mathbf{S}_{nh}(\mathbf{U}) & \text{(9a)} \\ \frac{\partial w}{\partial t} + u\frac{\partial w}{\partial x} = \frac{2p_{nh}}{h} & \text{(9b)} \\ h\frac{\partial (hu)}{\partial x} + 2hw - hu\frac{\partial}{\partial x}(h + 2z_b) = 0 & \text{(9c)} \end{cases}$$

where:

$$\mathbf{U} = \begin{pmatrix} h \\ hu \end{pmatrix}, \quad \mathbf{F}(\mathbf{U}) = \begin{pmatrix} hu \\ hu^2 + \frac{1}{2}gh^2 \end{pmatrix}, \quad \mathbf{S}_b(\mathbf{U}) = \begin{pmatrix} 0 \\ -gh\frac{\partial z_b}{\partial x} \end{pmatrix}, \quad \mathbf{S}_{nh}(\mathbf{U}) = \begin{pmatrix} 0 \\ -\left(h\frac{\partial p_{nh}}{\partial x} + p_{nh}\frac{\partial (h+2z_b)}{\partial x}\right) \end{pmatrix}, \tag{10}$$

2.2.1. Eigen-structure of the hyperbolic part of the HE-NHP system

As the numerical resolution of the hydrostatic part is carried out by means of a Roe-type solver, the eigen-structure of the system is of relevance. The hyperbolic system can be written in terms of its Jacobian matrix, $\mathbf{J}(\mathbf{U})$:

$$\frac{\partial \mathbf{U}}{\partial t} + \mathbf{J}(\mathbf{U})\frac{\partial \mathbf{U}}{\partial x} = \mathbf{S}_b(\mathbf{U}), \tag{11}$$

where $\mathbf{J}(\mathbf{U}) = \partial \mathbf{F}(\mathbf{U})/\partial \mathbf{U}$ can be diagonalized through the matrix $\mathbf{P}$, built with the Jacobian eigenvectors, $\mathbf{e}^m$:

$$\mathbf{J} = \mathbf{P}\mathbf{\Lambda}\mathbf{P}^{-1} \qquad \mathbf{P} = \begin{pmatrix} \mathbf{e}^1 & \mathbf{e}^2 \end{pmatrix} \tag{12}$$

providing the diagonal matrix $\mathbf{\Lambda}$ and the Jacobian eigenvalues λ^m:

$$\lambda^1 = u - c \qquad \lambda^2 = u + c \tag{13}$$

where $c = \sqrt{gh}$ stands for the celerity of surface waves in this model. The information waves are propagated over the eigenvectors basis, $\mathbf{e}^m$, that are

$$\mathbf{e}^1 = \begin{pmatrix} 1 \\ \lambda^1 \end{pmatrix}, \quad \mathbf{e}^2 = \begin{pmatrix} 1 \\ \lambda^2 \end{pmatrix}, \tag{14}$$

2.3. HR-NHP: hyperbolic relaxed non hydrostatic pressure model

Based on the artificial compressibility method, Escalante et al. [32] derived a hyperbolic relaxed system (HR-NHP) of equations for depth integrated non hydrostatic pressure model as

$$\begin{cases} \dfrac{\partial h}{\partial t} + \dfrac{\partial (hu)}{\partial x} = 0, & \text{(15a)} \\ \dfrac{\partial (hu)}{\partial t} + \dfrac{\partial}{\partial x}\left(\dfrac{(hu)^2}{h} + \dfrac{1}{2} g h^2 + (h p_{nh}) \right) = -(gh + 2p_{nh}) \dfrac{\partial z_b}{\partial x}, & \text{(15b)} \\ \dfrac{\partial (hw)}{\partial t} + \dfrac{\partial}{\partial x}\left(\dfrac{(hu)(hw)}{h} \right) = 2p_{nh}, & \text{(15c)} \\ \dfrac{\partial (hp_{nh})}{\partial t} + \dfrac{\partial}{\partial x}\left(\dfrac{(hu)(hp_{nh})}{h} \right) + k^2 \dfrac{\partial (hu)}{\partial x} + k^2 \left(-u \dfrac{\partial h}{\partial x} + 2w - 2u \dfrac{\partial z_b}{\partial x} \right) = 0. & \text{(15d)} \end{cases}$$

where $k = \alpha \sqrt{g H_0}$, being H_0 a reference depth and α a parameter that must be higher than 1 [32]. The parameter k can be interpreted as the wave speed in the depth integrated NHP system. Starting from the general celerity in a 1D elastic pipe [44]

$$\frac{1}{k^2} = \frac{\partial \rho}{\partial p} + \frac{\rho}{A} \frac{\partial A}{\partial p} \tag{16}$$

where A is the cross section, here assumed $A = h$, and considering density variations negligible

$$k^2 = \frac{h}{\rho} \frac{\partial p}{\partial h} \tag{17}$$

that, using $p/\rho = gh + p_{nh}$ and $\rho = 1$, gives

$$k^2 = gh + h \frac{\partial p_{nh}}{\partial h} \tag{18}$$

Therefore $k = \alpha \sqrt{g H_0}$ when $h \approx H_0$ and α is defined as

$$\alpha = \sqrt{1 + \frac{1}{g} \frac{\partial p_{nh}}{\partial h}} \tag{19}$$

This parameter introduces the information on p_{nh} variations with water depth. As p_{nh} is higher for higher h, the derivative will be always positive, ensuring that α is always higher than 1.

Note that (15d) contains the original DIIC (Eq. (9c)), derived from the divergence free condition:

$$\frac{\partial (hp_{nh})}{\partial t} + \frac{\partial}{\partial x}\left(\frac{(hu)(hp_{nh})}{h} \right) + k^2 \underbrace{\left(\frac{\partial (hu)}{\partial x} - u \frac{\partial h}{\partial x} + 2w - 2u \frac{\partial z_b}{\partial x} \right)}_{\text{DIIC}} = 0. \tag{20}$$

and, as pointed by Escalante [32], this equation can be seen as the transport of the divergence errors with a finite speed, k. Therefore, when $k \to \infty$, the original HE-NHP system (system (8)) is recovered. As expected, for $k = 0$ the hydrostatic SWE are recovered if an initial condition of $p_{nh} = w = 0$ is considered.

The HR-NHP system can be written in a compact form as:

$$\frac{\partial \mathbf{U}}{\partial t} + \frac{\partial \mathbf{F}(\mathbf{U})}{\partial x} + \mathbf{B}(\mathbf{U}) \frac{\partial \mathbf{U}}{\partial x} = \mathbf{S}_b(\mathbf{U}) + \mathbf{S}_{nh}(\mathbf{U}) \tag{21}$$

where the matrices are

$$\mathbf{U} = \begin{pmatrix} h \\ hu \\ hw \\ hp_{nh} \end{pmatrix} = \begin{pmatrix} h \\ q_u \\ q_w \\ q_p \end{pmatrix}, \quad \mathbf{F}(\mathbf{U}) = \begin{pmatrix} q_u \\ \frac{q_u^2}{h} + \frac{1}{2}gh^2 + q_p \\ \frac{q_u q_w}{h} \\ \frac{q_u q_p}{h} + k^2 q_u \end{pmatrix}, \quad \mathbf{S}_b(\mathbf{U}) = \begin{pmatrix} 0 \\ -(gh + 2p_{nh}) \\ 0 \\ 2k^2 u \end{pmatrix} \frac{\partial z_b}{\partial x},$$
$$\mathbf{S}_{nh}(\mathbf{U}) = \begin{pmatrix} 0 \\ 0 \\ 2p_{nh} \\ -2k^2 w \end{pmatrix}, \quad \mathbf{B}(\mathbf{U}) = \begin{pmatrix} 0 & 0 & 0 & 0 \\ 0 & 0 & 0 & 0 \\ 0 & 0 & 0 & 0 \\ -k^2 \frac{q_u}{h} & 0 & 0 & 0 \end{pmatrix}, \tag{22}$$

The Jacobian matrix of the physical fluxes, $\mathbf{J}_F = \frac{\partial \mathbf{F}(\mathbf{U})}{\partial \mathbf{U}}$, can be used to rewrite Eq. (21) as

$$\frac{\partial \mathbf{U}}{\partial t} + \mathbf{J}_F \frac{\partial \mathbf{U}}{\partial x} + \mathbf{B}(\mathbf{U}) \frac{\partial \mathbf{U}}{\partial x} = \mathbf{S}_b(\mathbf{U}) + \mathbf{S}_{nh}(\mathbf{U}) \tag{23}$$

or

$$\frac{\partial \mathbf{U}}{\partial t} + \mathbf{K}(\mathbf{U}) \frac{\partial \mathbf{U}}{\partial x} = \mathbf{S}_b(\mathbf{U}) + \mathbf{S}_{nh}(\mathbf{U}) \tag{24}$$

where matrix $\mathbf{K}(\mathbf{U})$ is

$$\mathbf{K}(\mathbf{U}) = \mathbf{J}_F + \mathbf{B}(\mathbf{U}) = \begin{pmatrix} 0 & 1 & 0 & 0 \\ c^2 - u^2 & 2u & 0 & 1 \\ -uw & w & u & 0 \\ -u(p_{nh} + k^2) & p_{nh} + k^2 & 0 & u \end{pmatrix}, \tag{25}$$

being c the same as in the hydrostatic shallow water system, $c = \sqrt{gh}$.

2.3.1. Eigen-structure of the system

The eigenvalues of matrix $\mathbf{K}(\mathbf{U})$ are:

$$\lambda^1 = u - C_e; \qquad \lambda^2 = u + C_e; \qquad \lambda^3 = \lambda^4 = u \tag{26}$$

where the new celerity, C_e, now contains information of the non-hydrostatic pressure: $C_e = \sqrt{gh + k^2 + p_{nh}}$. And, thus, the new eigenvectors are

$$\mathbf{e}^1 = \begin{pmatrix} 1 \\ \lambda^1 \\ w \\ k^2 + p_{nh} \end{pmatrix}, \quad \mathbf{e}^2 = \begin{pmatrix} 1 \\ \lambda^2 \\ w \\ k^2 + p_{nh} \end{pmatrix}, \quad \mathbf{e}^3 = \begin{pmatrix} 1 \\ u \\ 0 \\ -c^2 \end{pmatrix}, \quad \mathbf{e}^4 = \begin{pmatrix} 0 \\ 0 \\ 1 \\ 0 \end{pmatrix}, \tag{27}$$

Unlike the HE-NHP system, this model allows the explicit integration and the coupled resolution of the 4 variables at the same time. As a counterpoint, it is important to note that the definition of the celerity includes the variable k, which depends on the parameter α and the reference level H_0, leaving the numerical stability of the system dependent on an external parameter.

2.3.2. Linear dispersion relation of the system

The dispersive properties of the system are interesting to analyse for a better understanding of the results. Each system of equations has dispersive properties depending on the hypotheses on which its derivation is based, as summarized by Escalante and Morales de Luna [10], Busto et al. [13]. Dispersive analysis consists of a linearization of the system to find a solution that can be considered an approximate solution of the real system and, in this way, to find the velocity at which a system of equations propagates waves. The expression obtained for the propagation of the waves is compared with the theoretical one of the Stokes Linear Theory, giving information about the accuracy of the model that is solved.

The Linear Theory of Stokes (or Airy wave theory) [45] establishes a wave celerity over a still water volume depending on the wave number, k', as

$$C_{Airy}^2 = gH_0 \frac{\tanh(k'H_0)}{k'H_0} \tag{28}$$

where H_0 stands for the reference still water depth. The wide extended HE-NHP model has been analysed in other references [32,46] getting to an approximated celerity of

$$C_{HE-NHP}^2 = gH_0 \frac{1}{1 + \frac{1}{4}(k'H_0)^2}, \tag{29}$$

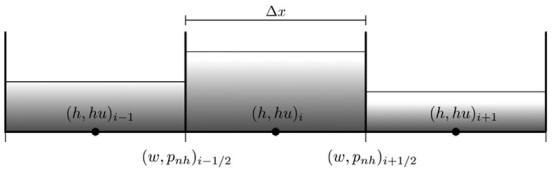

Fig. 1. Staggered grid and variable distribution for the HE-NHP numerical resolution.

while the celerity for the hyperbolized model has been also previously analysed [32] obtaining

$$C^2_{HR-NHP} = \left(\frac{J(k'H_0)+\gamma}{2} + \sqrt{\left(\frac{J(k'H_0)+\gamma}{2}\right)^2 - \gamma} \right)^{-1}, \tag{30}$$

where $J(k'H_0) = 1 + 1/4(k'H_0)^2$ and $\gamma = (k'H_0/2\alpha)^2$.

As pointed out by other authors, the error of phase velocity between these models and the Airy theory shows a good match when $k'H_0 \in [0,3]$. However, it is important to note that the celerity of HR-NHP system depends on α, and the tendency is to recover the original phase velocity of HE-NHP system (Eq. (29)) when α increases and $k \to \infty$. In particular, it is known that with $\alpha = 10$, the dispersive behaviour of HR model is quite similar to the HE-NHP model [32].

3. Numerical schemes

Both models are solved as an extension of a first-order explicit Roe-type Augmented Riemann Solver for the hyperbolic part.

3.1. Scheme for HE-NHP: explicit-Implicit finite volume method

To solve the hyperbolic-elliptic system, the *fractional time step* or *Pressure Correction Method* (PCM) [23] is applied. Splitting Eq. (9a) as

$$\underbrace{\frac{\partial \mathbf{U}}{\partial t} + \frac{\partial \mathbf{F}(\mathbf{U})}{\partial x} - \mathbf{S}_b(\mathbf{U})}_{\text{Hydrostatic}} = \underbrace{\mathbf{S}_{nh}(\mathbf{U})}_{\text{Non-hydrostatic}} \tag{31}$$

the system is solved in two steps: first, the hydrostatic part is solved; second, the variables are corrected with the non-hydrostatic pressure with the DIIC as condition.

As pointed in literature, this methodology, which is based on the correction of a preliminary velocity field, entails numerical problems that are frequently solved by means of staggered grids [22,23,28]. For instance, staggered grids have been usually applied to avoid check-board velocity distribution problems. For this reason, in HE-NHP model, the computational mesh, with NC cells and NW = NC + 1 walls, has the conserved variables h and hu defined at cell-centers, while variables w and p_{nh} are computed at cell edges, as depicted in Fig. 1.

3.1.1. Resolution of the hydrostatic part

The hydrostatic part is first solved up to an intermediate state: $\mathbf{U}^*$. At each cell edge $i+1/2$, located between cells i and $i+1$, Eq. (32) is locally linearized, giving rise to:

$$\frac{\partial \mathbf{U}}{\partial t} + \mathbf{J}(\widetilde{\mathbf{U}})\frac{\partial \mathbf{U}}{\partial x} = \mathbf{S}_b(\widetilde{\mathbf{U}}) \tag{32}$$

where the tilde variables stand for edge linearized vectors, in terms of averaged variables at cell edges -also represented with tilde). These averages, also known as Roe Averages, are obtained through the linearized Jacobian matrix, $\widetilde{\mathbf{J}}$, which fulfils:

$$\delta \mathbf{F} = \widetilde{\mathbf{J}} \delta \mathbf{U} \tag{33}$$

leading to the following average values of variables at cell edges:

$$\widetilde{h}_{i+1/2} = \frac{h_i + h_{i+1}}{2}, \qquad \widetilde{c}_{i+1/2} = \sqrt{g\widetilde{h}} \qquad \text{and} \qquad \widetilde{u}_{i+1/2} = \frac{u_{i+1}\sqrt{h_{i+1}} + u_i\sqrt{h_i}}{\sqrt{h_{i+1}} + \sqrt{h_i}}. \tag{34}$$

where subindexes $(.)_i$ and $(.)_{i+1}$ refer to cell values on the left and right side of every cell edge, respectively.

Note that all the scalars and vectors with tilde denote linearized values made from these averages. For instance, lambda values linearized at cell edges are $\widetilde{\lambda}^m = \widetilde{u} \pm \widetilde{c}$, where m stands for the wave components and runs from 1 to the number of Jacobian eigenvectors (2 in this case). For more details see Appendix B.2.

The system (32) is written for each computational cell, i, assuming an explicit first-order temporal discretization, and an upwind scheme for the spatial discretization of fluxes and source terms. The upwind discretization (superscripts $\pm$) allows discriminating the sign of information propagation:

$$\frac{\mathbf{U}_i^* - \mathbf{U}_i^n}{\Delta t} + \frac{\left[\tilde{\mathbf{P}}\tilde{\mathbf{\Lambda}}^+\left(\tilde{\mathcal{A}} - \tilde{\mathbf{\Lambda}}^{-1}\tilde{\mathcal{B}}\right)\right]_{i-1/2}^n + \left[\tilde{\mathbf{P}}\tilde{\mathbf{\Lambda}}^-\left(\tilde{\mathcal{A}} - \tilde{\mathbf{\Lambda}}^{-1}\tilde{\mathcal{B}}\right)\right]_{i+1/2}^n}{\Delta x} = 0 \tag{35}$$

being $\tilde{\mathcal{A}}$ and $\tilde{\mathcal{B}}$ the wave strengths and source terms vectors, respectively, whose construction is done through the eigenvectors inverse matrix, $\tilde{\mathbf{P}}^{-1}$, as

$$\tilde{\mathcal{A}} = \begin{pmatrix} \tilde{\alpha}^1 \\ \tilde{\alpha}^2 \end{pmatrix} = \tilde{\mathbf{P}}^{-1}\delta\tilde{\mathbf{U}} \qquad \text{and} \qquad \tilde{\mathcal{B}} = \begin{pmatrix} \tilde{\beta}^1 \\ \tilde{\beta}^2 \end{pmatrix} = \tilde{\mathbf{P}}^{-1}\tilde{\mathbf{S}}_b. \tag{36}$$

The particular definition of wave and source strengths can be seen in Eqs. (B.33) and (B.34) in Appendix B.3.

And for each particular variable, the updating scheme to the intermediate state, is

$$h_i^* = h_i^n - \frac{\Delta t}{\Delta x}\left[\sum_m \left(\tilde{\lambda}^+\tilde{\gamma}\tilde{\mathbf{e}}_1\right)_{i-1/2}^m + \sum_m \left(\tilde{\lambda}^-\tilde{\gamma}\tilde{\mathbf{e}}_1\right)_{i+1/2}^m\right] \tag{37}$$

$$(hu)_i^* = (hu)_i^n - \frac{\Delta t}{\Delta x}\left[\sum_m \left(\tilde{\lambda}^+\tilde{\gamma}\tilde{\mathbf{e}}_2\right)_{i-1/2}^m + \sum_m \left(\tilde{\lambda}^-\tilde{\gamma}\tilde{\mathbf{e}}_2\right)_{i+1/2}^m\right], \tag{38}$$

where $\tilde{\gamma}_{i+1/2}^m = \left(\tilde{\alpha}^m - \frac{\tilde{\beta}^m}{\tilde{\lambda}^m}\right)_{i+1/2}$.

Before starting the non-hydrostatic pressure computation, the hydrostatic part of Eq. (9b) is also solved up to the intermediate state *, computing it as a transported scalar w at velocity u:

$$w_{i+1/2}^* = w_{i+1/2}^n - \frac{\Delta t}{\Delta x}\left[(u\delta w)_i^+ + (u\delta w)_{i+1}^-\right]. \tag{39}$$

Note that this vertical velocity is solved at cell edges, $i+1/2$, instead of cell centers due to the staggered grid and, thus, fluxes are evaluated at cell centers, i and $i+1$.

In all the above computations, the time step size is restricted by the CFL condition to ensure numerical stability as

$$\Delta t = \mathrm{CFL}\frac{\Delta x}{\max|\tilde{\lambda}|_i^n} \tag{40}$$

where the CFL is a dimensionless number that must be between 0 and 1.

The present model gives special care to wet/dry fronts through enforcing positive values of interface discrete water depths, following the methodology of previous work [40,41]. The algorithm computes some intermediate states at cell interfaces and, when they are negative, flux splitting contribution bounces from the dry cell back to the wet cell, as also applied to a shallow water model in Echeverribar et al. [35]. As the non-hydrostatic part acts as a correction over the wet field, no additional correction is needed.

3.1.2. Resolution of the non-hydrostatic part

The intermediate variables would be the definitive values for the next time step if the pressure was hydrostatic. However, the velocity field has to be corrected to fulfil the DIIC through the non-hydrostatic pressure terms as:

$$h_i^{n+1} = h_i^* \tag{41}$$

$$(hu)_i^{n+1} = (hu)_i^* + \mathcal{Q}(p_{nh}) \tag{42}$$

$$(w)_{i+1/2}^{n+1} = (w)_{i+1/2}^* + \mathcal{W}(p_{nh}) \tag{43}$$

using:

$$\mathcal{Q}(p_{nh}) = -\Delta t\left[h_i^{n+1}\frac{p_{nh,i+1/2}^{n+1} - p_{nh,i-1/2}^{n+1}}{\Delta x} + p_{nh,i}^{n+1}\frac{(h+2z_b)_{i+1}^{n+1} - (h+2z_b)_{i-1}^{n+1}}{2\Delta x}\right] \tag{44}$$

$$\mathcal{W}(p_{nh}) = \Delta t\frac{2p_{nh,i+1/2}^{n+1}}{h_{i+1/2}^{n+1}} \tag{45}$$

They are introduced in Eq. (9c) leading to a Poisson equation:

$$\left[h_{i+1/2} \frac{(hu)_{i+1} - (hu)_i}{\Delta x} + 2h_{i+1/2} w_{i+1/2} - (hu)_{i+1/2} \frac{\left(h_{i+1} + 2z_{b,i+1} - h_i - 2z_{b,i}\right)}{\Delta x} \right]^{n+1} = 0 \tag{46}$$

Reordering:

$$A_{i+1/2} \mathbf{P}^{n+1}_{nh,i-1/2} + B_{i+1/2} \cdot \mathbf{P}^{n+1}_{nh,i+1/2} + C_{i+1/2} \cdot \mathbf{P}^{n+1}_{nh,i+3/2} = D_{i+1/2} \tag{47}$$

where coefficients A, B, C and D can be seen in detail in Appendix B.1. To solve this equation, an implicit numerical scheme must be used. In this case, the Thomas Algorithm or tridiagonal matrix algorithm is applied [22]. Once this equation is solved, the new NH pressure field is obtained and the rest of variables can be updated with this pressure following (42)–(45).

The numerical scheme fulfils the C-property as the SW part is solved with a well-known scheme already tested and the non-hydrostatic approach also ensures the equilibrium. The details of the demonstration can be seen in Appendix B.4.

3.2. Scheme for HR-NHP: fully-explicit finite volume method

As system (15) is fully coupled, the Roe-approach can be extended and new Roe-averages must be computed. For that purpose, the matrix form is useful

$$\frac{\partial \mathbf{U}}{\partial t} + \mathbf{K}(\widetilde{\mathbf{U}}) \frac{\partial \mathbf{U}}{\partial x} = \mathbf{S}_b(\mathbf{U}) + \mathbf{S}_{nh}(\mathbf{U}) \tag{48}$$

where $\mathbf{K}(\widetilde{\mathbf{U}}) = \mathbf{J}_F(\widetilde{\mathbf{U}}) + \mathbf{B}(\widetilde{\mathbf{U}})$, and tilde again refers to the linearized values at cell edges. Those averaged values inside matrix $\mathbf{K}(\widetilde{\mathbf{U}})$ ensure a proper discretization of the system [47]. The new Roe-averages at wall $i+1/2$ for vertical velocity, w, and non-hydrostatic pressure, p_{nh} are

$$\widetilde{p}_{nh,i+1/2} = \frac{p_i h_i \sqrt{h_{i+1}} + p_{i+1} h_{i+1} \sqrt{h_i}}{h_{i+1}\sqrt{h_i} + h_i \sqrt{h_{i+1}}}, \qquad \widetilde{w}_{i+1/2} = \frac{w_i h_i \sqrt{h_{i+1}} + w_{i+1} h_{i+1} \sqrt{h_i}}{h_{i+1}\sqrt{h_i} + h_i \sqrt{h_{i+1}}} \tag{49}$$

where subindexes $(.)_i$ and $(.)_{i+1}$ refer to cell values on the left and right side of the cell edge, respectively. The derivation of these values can be found in (B.35) and (B.36) in B.2.

The final updating expression is

$$\mathbf{U}_i^{n+1} = \mathbf{U}_i^n - \frac{\Delta t}{\Delta x} \left[\sum_{m=1}^{4} \left(\tilde{\lambda}^+ \tilde{\gamma} \tilde{\mathbf{e}} \right)^m_{i-1/2} + \sum_{m=1}^{4} \left(\tilde{\lambda}^- \tilde{\gamma} \tilde{\mathbf{e}} \right)^m_{i+1/2} \right] + \Delta t \mathbf{S}_{nh}(\mathbf{U})_i^{n+1}, \tag{50}$$

3.2.1. Source term discretization

Note that bed slope source terms are incorporated to the wave structure evaluating them at cell edges, whereas the $\mathbf{S}_{nh}(\mathbf{U})$ has been discretized cell centered. In particular, this last source term can be evaluated at different times leading to different consequences on numerical results. Depending on this, two different approaches are analysed in this work:

A pure explicit discretization of this term can be applied when all the terms are evaluated at $t = t^n$, having

$$(q_w)_i^{n+1} = (q_w)_i^* + \Delta t \frac{2(q_p)_i^n}{h_i^n} \qquad (q_p)_i^{n+1} = (q_p)_i^* - \Delta t \frac{2k^2 (q_w)_i^n}{h_i^n} \tag{51}$$

being the asterisk the representation of the conserved variables updated with upwind contributions. When this formulation is used, the source term is called $\mathbf{S}_{nh}^{\exp}$.

On the other hand, if the term is evaluated at $n+1$, q_w and q_p are updated as follows:

$$(q_w)_i^{n+1} = (q_w)_i^* + \Delta t \frac{2(q_p)_i^{n+1}}{h_i^{n+1}} \qquad (q_p)_i^{n+1} = (q_p)_i^* - \Delta t \frac{2k^2 (q_w)_i^{n+1}}{h_i^{n+1}} \tag{52}$$

Thus, as each of the variables depends on the other, the final updating scheme yields

$$(q_w)_i^{n+1} = \frac{(q_w)_i^* + 2\Delta t \frac{(q_p)_i^*}{h_i^{n+1}}}{1 + \Delta t^2 \frac{2(q_p)_i^{n+1}}{(h_i^{n+1})^2}} \qquad (q_p)_i^{n+1} = (q_p)_i^* - \Delta t \frac{2k^2 (q_w)_i^{n+1}}{h_i^{n+1}} \tag{53}$$

This implicit formulation of the source term is named $\mathbf{S}_{nh}^{imp}$ in the present work. It is important to note that this local implicit formulation of source term does not alter the explicitness of the scheme.

It is worth mentioning that the term $\mathbf{S}_{nh}(\mathbf{U})$ deeply governs the behaviour of the model, as it is the feedback of z momentum and non-hydrostatic pressure equations. Therefore, the model presents a high sensitivity to the way of discretizing this term. Its explicit discretization provides very unstable results, while its evaluation at $n+1$ is more stable. A more detailed assessment of the consequences of discretization is done in the solitary wave test case, in Section 4.

Finally, due to the explicit character of the main scheme, the time step size is also limited by the CFL condition to avoid numerical instabilities. It can be dynamically computed according to the new eigenvalues:

$$\Delta t = \text{CFL}\frac{\Delta x}{\max|\widetilde{\lambda}|_i^n} \rightarrow \quad \Delta t = \text{CFL}\frac{\Delta x}{\max\left|\left(\tilde{u} \pm \sqrt{\tilde{c}^2 + k^2 + \tilde{p}_{nh}}\right)\right|_i^n}, \qquad \text{CFL} \leq 1 \tag{54}$$

Note that, the time step Δt is also restricted by celerities that depend on parameter α through the k value.

The numerical scheme is well balanced and the demonstration can be seen in Appendix B.4. Finally, the wetting and drying algorithm follows the same control as the hydrostatic part of the HE-NHP model. By using intermediate states of water depth that must be always positive, the decision of performing a usual flux splitting is carried out.

4. Numerical validation: solitary wave propagation

A solitary wave is a wave which propagates without any change in shape from a reference moving with its group velocity. From a mathematical point of view, the solitary wave is the solution of equations where dispersive effects compensate nonlinear effects, producing a shape maintenance. Many models have soliton-kind solutions [48], for instance, the Korteweg-de-Vries equation [46]. However, although the real and exact solutions are always limited by the conditions assumed to derive each model, in fluid mechanics, the solitary wave is a standard solution to test the properties of the models [28,49,50].

The standard solitary wave has a surface level, $h(x,t)$, governed by Bristeau et al. [21], Escalante et al. [50]

$$h(x,t) = H_0 + A\text{sech}^2\left[\frac{1}{H_0}\sqrt{\frac{\gamma A}{A+H_0}}(x-ct)\right] \tag{55}$$

where A is the wave amplitude, H_0 stands for the unperturbed level and c is the propagating velocity of the wave. The γ parameter allows to choose between $\gamma = 2$, for the NH model, and $\gamma = 3/2$ for the Serre–Green–Naghdi model [50]. In this work, $\gamma = 2$ is used. The celerity, c, is modelled as in many references [28,46,49,50] following: $c = \sqrt{g(A+H_0)}$. The horizontal depth-averaged velocity is given by

$$u(x,t) = c\left(1 - \frac{H_0}{h(x,t)}\right). \tag{56}$$

Some references use this reference solution as initial condition setting $h(x,0)$ and $u(x,0)$ based on (55) and (56) and assuming $w = p_{nh} = 0$ [28,49]. However, some others complete the initial condition with an expression for vertical velocity [50] or even for NH pressure [21]. In this work the complete initial condition has been used, defining w and p_{nh} as

$$w(x,t) = \frac{-cA}{h(x,t)}\sqrt{\frac{\gamma A}{A+H_0}}\text{sech}^3\left(\frac{1}{H_0}\sqrt{\frac{\gamma A}{A+H_0}}(x-ct)\right)\sinh\left(\frac{1}{H_0}\sqrt{\frac{\gamma A}{A+H_0}}(x-ct)\right) \tag{57}$$

$$\begin{aligned} p_{nh}(x,t) = \frac{(cA)^2}{2(A+H_0)h(x,t)}\Bigg[&\frac{2A}{h(x,t)}\text{sech}^6\left(\frac{1}{H_0}\sqrt{\frac{\gamma A}{A+H_0}}(x-ct)\right)\sinh^2\left(\frac{1}{H_0}\sqrt{\frac{\gamma A}{A+H_0}}(x-ct)\right) \\ &-3\text{sech}^3\left(\frac{1}{H_0}\sqrt{\frac{\gamma A}{A+H_0}}(x-ct)\right)\sinh^2\left(\frac{1}{H_0}\sqrt{\frac{\gamma A}{A+H_0}}(x-ct)\right) + \text{sech}^2\left(\frac{1}{H_0}\sqrt{\frac{\gamma A}{A+H_0}}(x-ct)\right)\Bigg] \end{aligned} \tag{58}$$

It is worth noting that there is always an error associated to the estimation of celerity, c.

A solitary wave of $A = 0.01$ m and $H_0 = 1$ m is propagated in this work using both models (HE and HR). The initial condition locates the center of the perturbation wave at $x = 100$ m of a flat channel. This test case is used to asses two different issues: first, the proper numerical discretization of $\mathbf{S}_{nh}$ source term in HR-NHP model in Section 4.1; next, the solitary wave is propagated with the selected discretization (implicit) to perform a convergence analysis.

4.1. Sensitivity analysis to discretization of source terms in NH-NHP model

This section is devoted to show the importance of a proper discretization of $\mathbf{S}_{nh}(\mathbf{U})$, as it governs the flow and can directly turn the model into unstable. Depending on the formulation of the source term: implicit, $\mathbf{S}_{nh}^{imp}$, or explicit, $\mathbf{S}_{nh}^{\exp}$, the scheme presents a very different numerical behaviour.

To demonstrate it, the described solitary wave is propagated with both approaches in HR model. In both cases, the computational mesh has 5000 cells and $\alpha = 7$. When using $\mathbf{S}_{nh}^{imp}$, the CFL number is set to 1.0 and the simulation can run

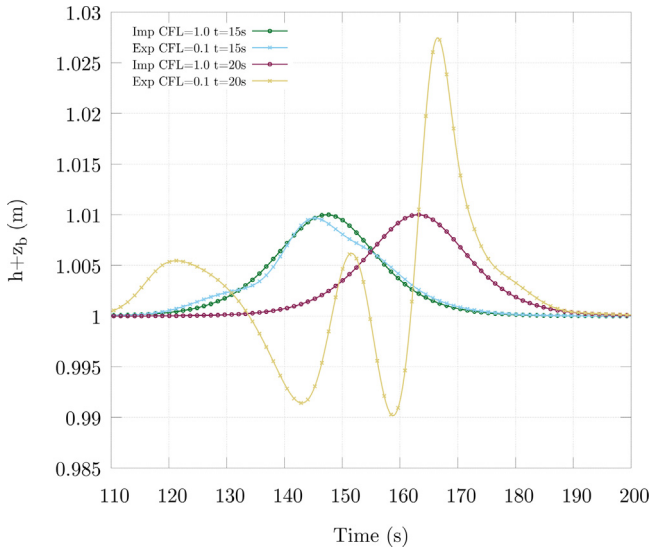

Fig. 2. Comparison between reference soliton and numerical results for HE-NHP model at time $t = 20$ s.

up to the end. However, when modelling with $\mathbf{S}_{nh}^{\text{exp}}$, the CFL number needs to be decreased to 0.1 to be able to run up to $t = 20$ s without huge instabilities. In Fig. 2, both simulations with both models can be seen at two different times: $t = 15$ s and $t = 20$ s. It can be seen that, while $\mathbf{S}_{nh}^{\text{exp}}$ formulation propagates the solitary wave without perturbation using the highest CFL number, the $\mathbf{S}_{nh}^{imp}$ starts to change its shape at $t = 15$ s and gets unstable at $t = 20$ s, although using a very low CFL number.

Additionally, it is important to note that the simulated case is favourable to the numerical stability, and results can be more unstable when using $\mathbf{S}_{nh}^{\text{exp}}$ increasing α, increasing the CFL or reducing the mesh refinement. Therefore, although some cases can be simulated with $\mathbf{S}_{nh}^{\text{exp}}$ if low CFL numbers are used, the rest of the work is presented with $\mathbf{S}_{nh}^{imp}$, which is robust and fast.

4.2. Convergence analysis

The solitary wave is propagated over a flat channel 600 m long during 100 s and the numerical solutions are compared against the reference solution from Eq. (55). It must be noticed that (55) is not an exact solution of the system (8) and (24), only an approximated one due to the estimation of wave celerity. Different number of cells in six computational meshes are tested in order to carry out a convergence analysis with each model involving 312, 625, 1250, 2500, 5000 and 10,000 cells. The HR-NHP model is used with different wave speeds, $k = \alpha\sqrt{gH_0}$, using $\alpha = 3$, 5, and 10. All the simulations have been performed with CFL = 1.0.

In Fig. 3 the comparison of the reference and the numerical solutions with all the meshes can be seen for the HE-NHP model at time $t = 20$ s in terms of surface elevation. It can be observed how the coarsest mesh (Mesh 1, with 312 cells) shows huge discrepancies with the reference solution in terms of wave width and amplitude, due to numerical diffusion. As the refinement increases up to Mesh 6, with 10,000 cells, the results present better agreement with the reference soliton. A detail of the results can be seen in the zoom of Fig. 3. It is important to note that this reference soliton estimates a celerity and is not an exact solution of the system, thus, the finest solution presents a small deviation in terms of amplitude that can be seen in the. This leads to a limit in the error decrease, that can not be improved although the mesh could still be refined.

Finally, it is worth mentioning that the wave propagation computed using the reference solution with $\gamma = 3/2$, instead of using $\gamma = 2$, could be an acceptable comparison. However, as it is not the solution of the NH system but the Serre-Green–Naghdi, delays in results with respect to the reference solitary wave would appear, besides the discrepancies provoked by the c estimation.

This error limit can be also seen in Table 1, where the L_1 norm and order are calculated for all the models and meshes. For each refinement, the reference solution is projected over the mesh and results are compared cell by cell and model by model. In all the cases, the theoretical convergence order is achieved as the numerical scheme is first order. Additionally, in all the models, the propagation of the solitary wave without perturbing its shape denotes the proper dispersive behaviour of the system, which is able to compensate the non-linear effects that tend to sharp the wave peak.

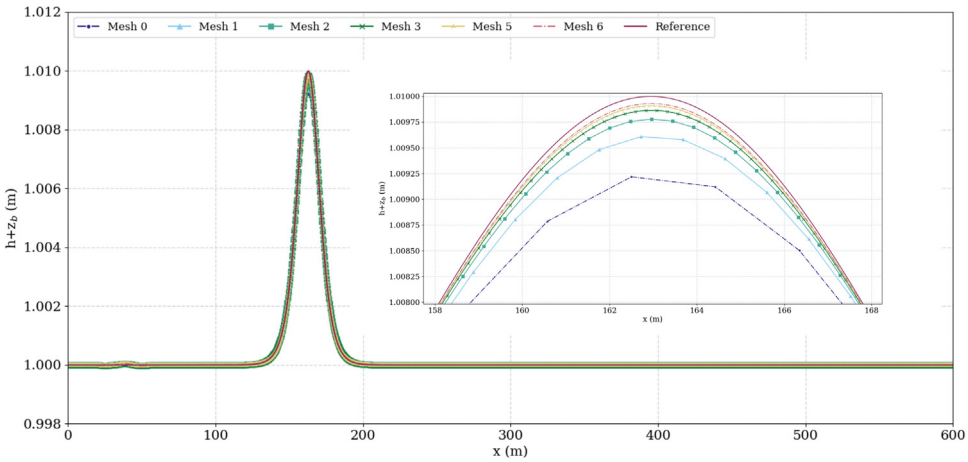

Fig. 3. Comparison between reference soliton and numerical results for HE-NHP model at time $t = 20$ s.

Table 1
L1 norm and order computed for each model simulating the solitary wave at time $t = 20$ s.

L_1 norm					
Mesh	N cells	HE	HR ($\alpha = 3$)	HR ($\alpha = 5$)	HR ($\alpha = 10$)
1	312	2.252506e−05	3.290751e−05	4.344987e−05	6.922845e−05
2	625	1.166959e−05	1.660781e−05	2.319174e−05	3.832115e−05
3	1250	7.167602e−06	9.636071e−06	1.285504e−05	2.113940e−05
4	2500	4.844605e−06	6.114220e−06	7.765850e−06	1.209022e−05
5	5000	3.694948e−06	4.346192e−06	5.181070e−06	7.391345e−06
6	10000	3.132846e−06	3.459860e−06	3.877911e−06	4.994991e−06
			Order		
Mesh	N cells	HE	HR ($\alpha = 3$)	HR ($\alpha = 5$)	HR ($\alpha = 10$)
1	312	–	–	–	–
2	625	0.9954	0.9480	0.8707	0.7930
3	1250	0.8938	0.8943	0.8704	0.8189
4	2500	0.8189	0.8452	0.8477	0.8274
5	5000	0.7322	0.7809	0.8064	0.8181
6	10000	0.6418	0.7038	0.7458	0.7874

5. Results for steady flow

Numerical model validation is often performed by comparing with analytical solutions or exact solutions when available. However, as this is the case for any complex system of equations such as the present one, the exact solution cannot be obtained unless certain assumptions are made, such as steady flow. In [21], a solution is provided for stationary non-hydrostatic flows, derived from system (9) (HE-NHP). They refer to it as *quasi-analytical* system, since it contains a few ODEs, which can be easily solved numerically. In this work, the same approach is also applied to the HR-NHP model to get a new steady reference solution to compare with, derived from (15). Both systems are next presented and used as reference solutions.

If a constant discharge, Q_0, a water depth boundary condition, H_0, and a function for the average vertical velocity, $w(x)$, are set; the variables $p_{nh}(x)$, $h(x)$, $u(x)$ and $z_b(x)$ can be calculated. For both models (HE-NHP and HR-NHP), the average vertical velocity function assumed is:

$$w(x) = c(x-a)\exp(-b(x-a)^2) \tag{59}$$

where a, b and c are constant parameters. The system is solved with the *odeint Python* library and used as reference solution. In this work, two different cases are analysed in order to asses two scenarios with different properties. In Table 2, the parameters chosen for each case are summarized.

Table 2
Parameters of the two reference solution steady cases.

	H_0	Q_0	z_0	a	b	c
Case 1	1.0	0.5	0.0	5.0	5.0	1.0
Case 2	1.0	1.8	0.0	5.0	3.4	3.0

5.1. HE-NHP steady reference solution

In the case of the HE-NHP model, the simplification of system (9) neglecting temporal derivatives leads to the steady system:

$$\begin{cases} u = \dfrac{Q_0}{h} & \text{(60a)} \\ p_{nh} = \dfrac{Q_0}{2}\dfrac{\partial w}{\partial x} & \text{(60b)} \\ \left(1/2gh - Q_0^2/h^2\right)\dfrac{dh}{dx} = -\dfrac{h}{Q_0}\left(gh + Q_0\dfrac{dw}{dx}\right)w - \dfrac{Q_0}{2}h\dfrac{d^2w}{dx^2} & \text{(60c)} \\ \dfrac{dz_b}{dx} = -\dfrac{1}{2}\dfrac{dh}{dx} + \dfrac{hw}{Q_0} & \text{(60d)} \end{cases}$$

In Fig. 4, the x-profile of the variables is plotted for case 1 and 2. Note that the input of the algorithm is the vertical velocity function (59), that is only non-zero in the center of the domain. Thus, the flow at the boundaries is purely hydrostatic, pressure is nil and no vertical perturbations appear.

5.2. HR-NHP steady reference solution

The former subsection presents a system already derived in Bristeau et al. [21]. Additionally, in this work a new steady system is derived for the non-hydrostatic relaxed system (HR-NHP), in order to understand the behaviour of the system when some of the parameters vary.

If system (15) is simplified to become steady, the variables $p_{nh}(x)$, $h(x)$, $u(x)$ and $z_b(x)$ are also defined for given boundary condition: Q_0, H_0; and for a given average vertical velocity profile, $w(x)$, as in definition (59). In this case, the steady system is

$$\begin{cases} u = \dfrac{Q_0}{h} & \text{(61a)} \\ p_{nh} = \dfrac{Q_0}{2}\dfrac{dw}{dx} & \text{(61b)} \\ \left(1/2gh - Q_0^2/h^2\right)\dfrac{dh}{dx} = -\dfrac{d^2w}{dx^2}\dfrac{Q_0h}{4k^2}\left(2k^2 + gh + Q_0\dfrac{dw}{dx}\right) - g\dfrac{h^2w}{Q_0} - hw\dfrac{dw}{dx} & \text{(61c)} \\ \dfrac{dz_b}{dx} = \dfrac{Q_0h}{4k^2}\dfrac{d^2w}{dx^2} - \dfrac{1}{2}\dfrac{dh}{dx} + \dfrac{hw}{Q_0} & \text{(61d)} \end{cases}$$

Note that system (61) has the same definition for vertical velocity and non-hydrostatic pressure as system (60). However, the equations for bottom, z_b and water depth, h, now contain terms depending on parameter k which, therefore, determines the solution of the system. However, it is worth mentioning that for higher k values, the solutions for system (61) and (60) are more similar. Figs. 5 and 6 show the solution of system (61) for cases 1 and 2, respectively. Both figures plot the variable distribution for different α values: 1.6, 3, 5 and 10. In case 1, with a smoother $w(x)$ distribution, the variations of α are not noticeable. However, in case 2, the same vertical velocity distribution generates different water depths and horizontal velocities depending on α. Nevertheless, it is worth noting that the solution converges as α increases.

5.3. Numerical steady results

In this case, the exact z_b distribution is set as topography and used to simulate the convergence to a steady state with both models: HE-NHP and HR-NHP. The initial condition is the quasi-analytical solution for each model projected over the computational mesh. The steady discharge is set as inlet boundary condition, while the still water depth is set as outlet boundary condition.

In both cases, computational meshes contain 1000 cells with equidistant centers and edges -where w and p_{nh} are computed for HE-NHP model. All the simulations have been carried out with CFL = 1.0.

Figs. 7 and 8 show the numerical results for cases 1 and 2, respectively, provided by the HE-NHP model -in brown- and for a hydrostatic shallow water (SW) model -in green-. It is worth mentioning that the results with the SW model are not in agreement with the reference solution as expected, since the reference is not a solution of the SW system of equations.

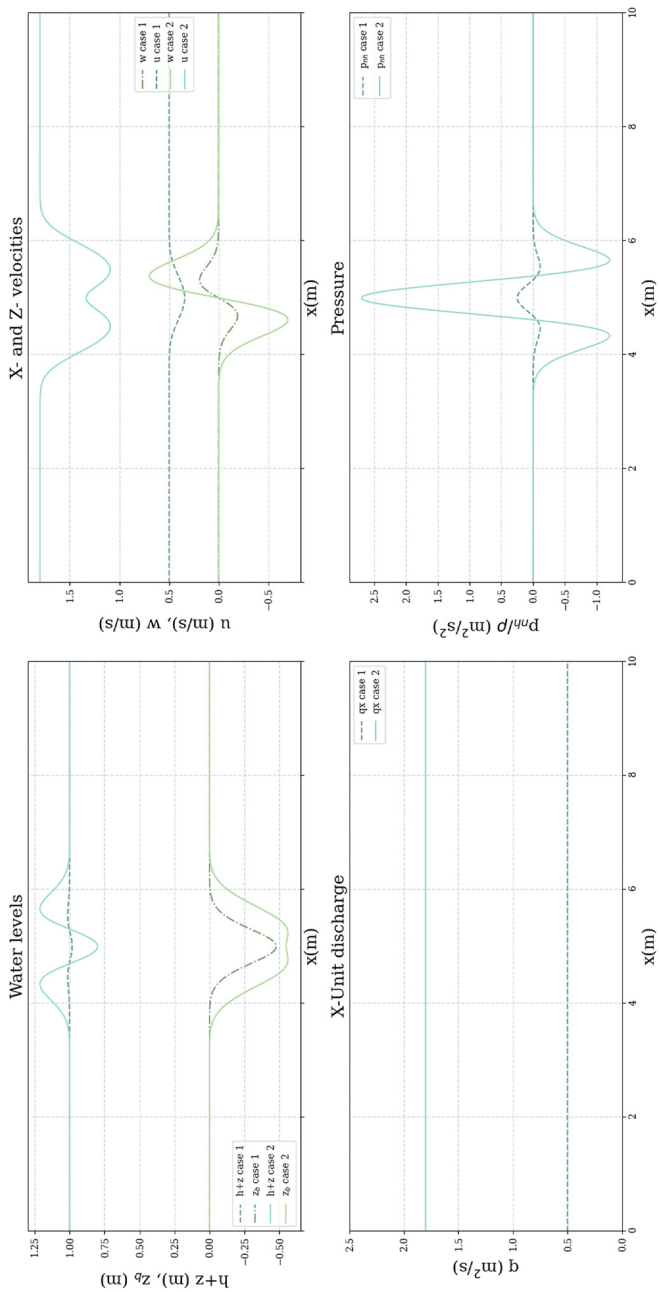

Fig. 4. Variables distribution comparison of cases 1 and 2 in the reference solution for steady state in the HE-NHP model.

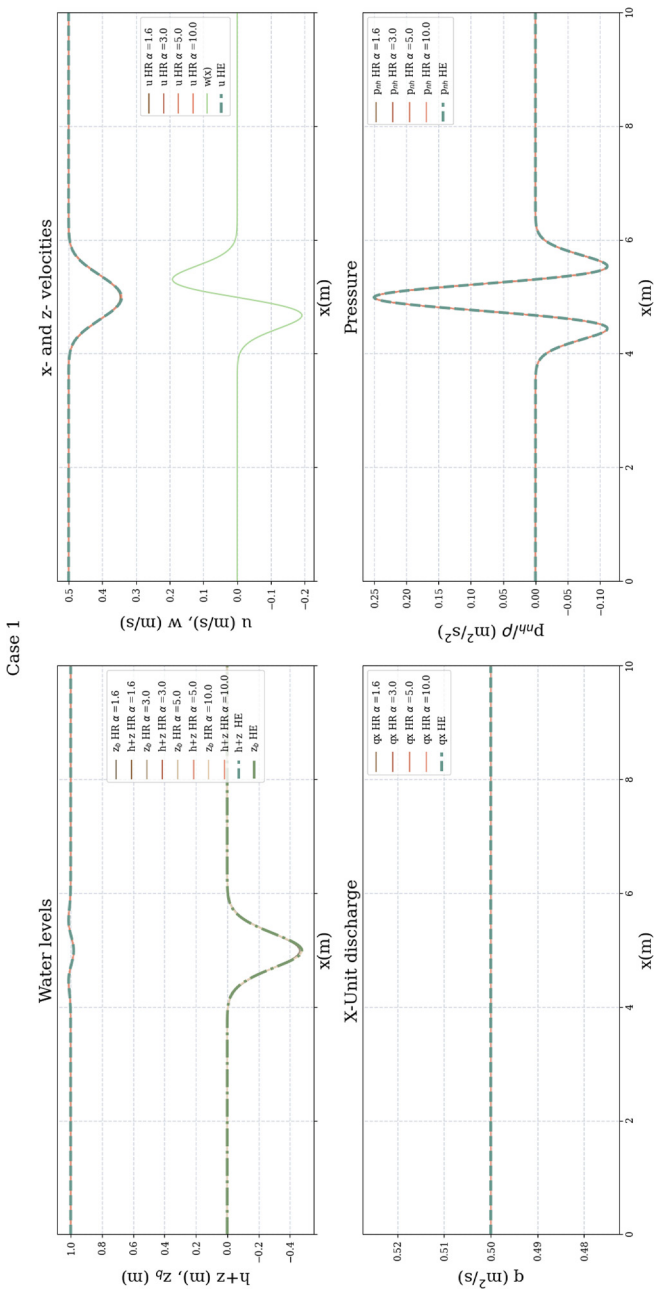

Fig. 5. Variables distribution in the reference solution for steady state in HR-NHP system for case 1.

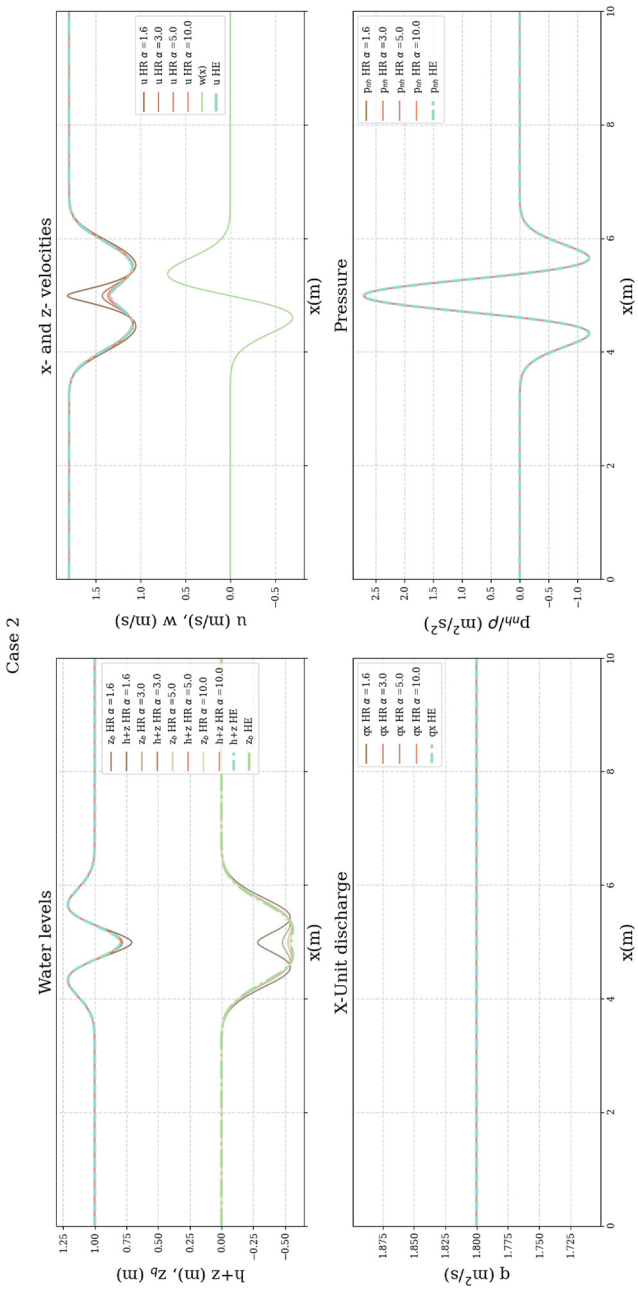

Fig. 6. Variables distribution in the reference solution for steady state in HR-NHP system for case 2.

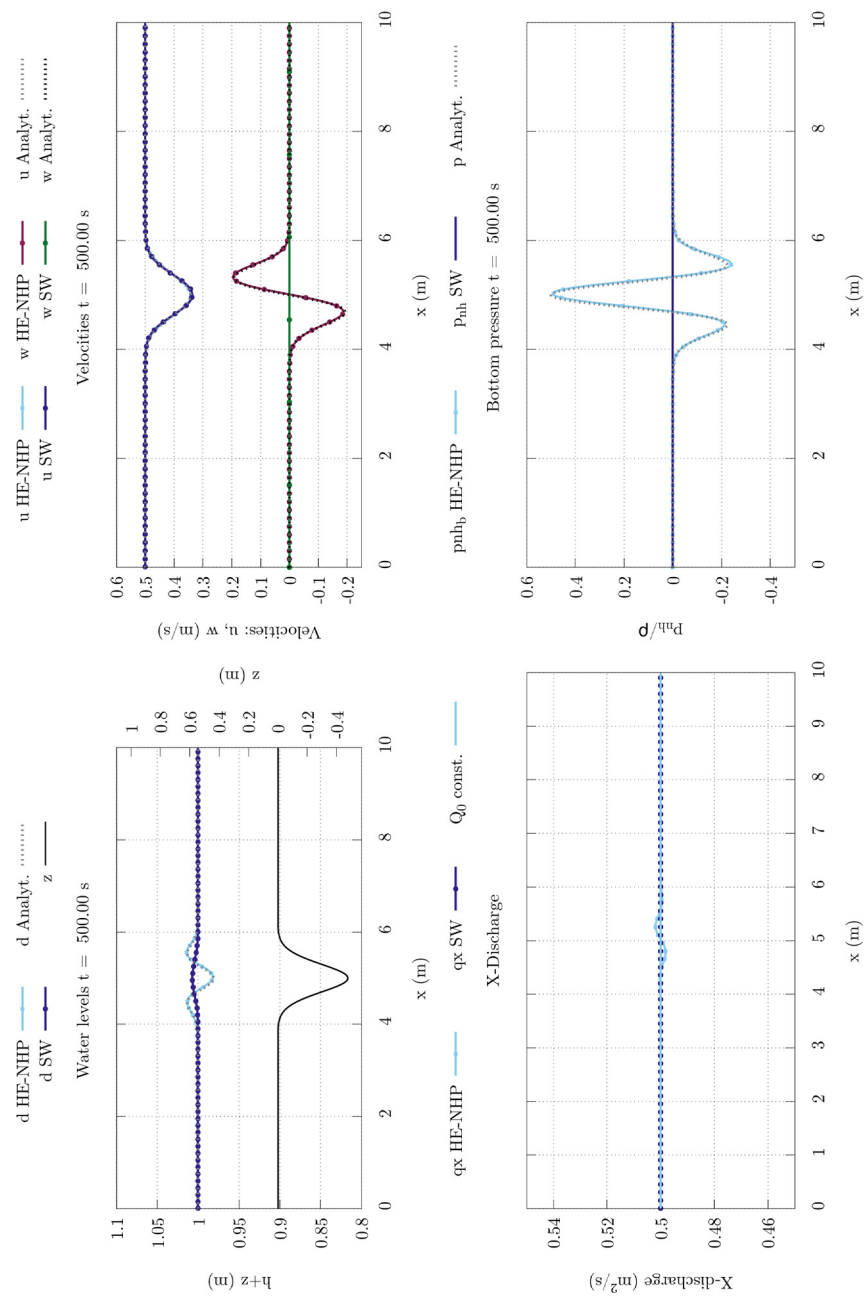

Fig. 7. Variables distribution in the numerical solution for steady case 1 with HE-NHP.

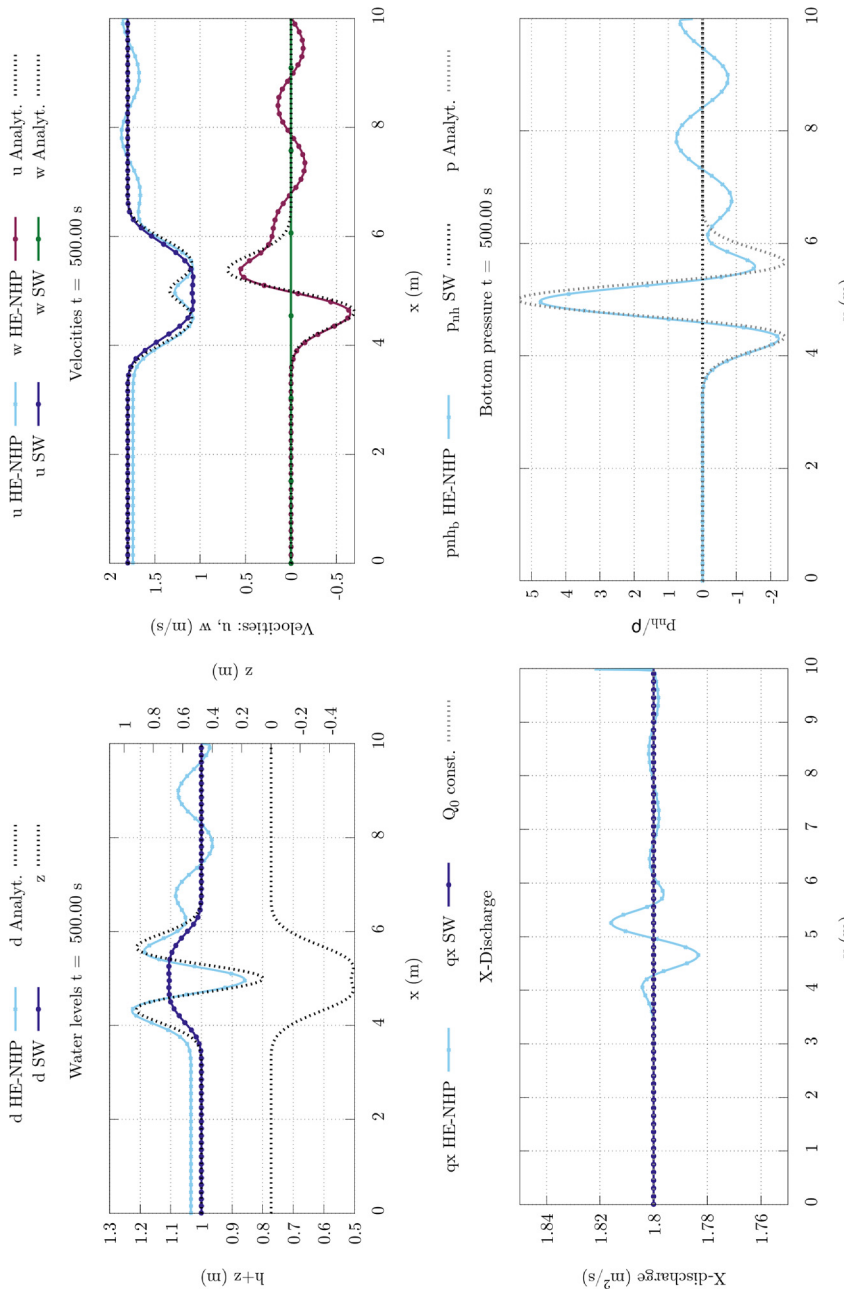

Fig. 8. Variables distribution in the numerical solution for steady case 2 with HE-NHP.

The hydrostatic solution is only plotted to compare the behaviour of the depth-averaged model when including the non-hydrostatic effects. Both models (HE-NHP and SW) share the hydrostatic part so that the SW model works as the HE-NHP model without the pressure correction algorithm.

First, it is noted that, with a SW hydrostatic model, the correct surface curvature is not captured for a bottom like the one given in either case. Of course, vertical pressure and velocity distributions are not even contemplated in the hydrostatic case. Second, a typical behaviour of non-hydrostatic pressure models is observed when there are regime changes in steep bottoms, which is the generation of static wave trains [9]. This behaviour is more noticeable in case 2, where the change is more abrupt than in case 1. Additionally, a non-uniform distribution of discharge in the non-zero vertical velocity areas is present for the same reason. Therefore, the HE-NHP model is demonstrated to have the same dispersive behaviour as other DSW and NHP models [9]. Despite that fact, the HE-NHP model presents an accurate resolution of the surface variations and pressure distribution on these steady states.

The same simulations are carried out with the HR-NHP model, but testing different values of the α parameter. As reported in Escalante et al. [32], boundary reflections might generate undesirable results inside the domain. To avoid it, absorbing boundary conditions are widely used [32]. In this test case, in addition to a discharge as inlet, a constant level as outlet and $p = w = 0$ at inlet boundary conditions, $p_{nh} = 0$ at the outlet is set to improve the results for lower values of α. Although each α value generates a different bottom, all the cases have been simulated with the bottom generated with $\alpha = 10.0$, as the bottom is almost the same when this parameter increases. The biggest discrepancies can be found between the bottom generated with $\alpha = 3$, and that of $\alpha = 10.0$. In fact, the results with $\alpha = 3$ could be more accurate if the simulation would had run with a reference bottom calculated with $\alpha = 3$. However, as can be seen in Figs. 9 and 10, that show the numerical results for cases 1 and 2, respectively, all the simulation with different values of the parameter present similar results. As in the HE-NHP system, the behaviour is quite similar, presenting good results in case 1 and those dispersive oscillations in case 2.

6. Results for unsteady flow: wave propagation over a bottom bar

In [51] a laboratory experiment was performed to analyse and measure the phenomenon of shape and frequency transformation of waves traveling over submerged bars. The surface perturbation, η -the difference between water depth and mean water level at rest-, provoked by a boundary wave was registered at 8 probes. Terrain variations were demonstrated to provoke the significant wave variations. In particular, the experimental work divides the studied waves into long and short waves, that behave differently depending on the wavelength. Additionally, the work focuses on the effect of the breaking process, which generates an energy dissipation that must be taken into account with additional models, as reported by Castro-Orgaz and Chanson [8], Tonelli and Petti [49].

In this work, the long non-breaking wave experiment -termed SLN by the experiment's authors- is simulated, as it presents an interesting amplification of the bound harmonics during the shoaling process, and their release in the deeper regions develops a wave decomposition that only a dispersive model is able to reproduce. The results of these experiments have been used as validation benchmark test cases of NHP and DSW models [28,52], as hydrostatic SW models are not able to reproduce the generation of high frequency waves.

In Fig. 11 a sketch of the channel is shown. The gauging points are marked with vertical lines and labeled with a number. Probe 1 corresponds to the intersection between the bottom bar starting point and the flat bottom. The probes register the evolution of waves in terms of η while they propagate through deep and shallow zones.

The experimental case is simulated with the three different models: pure hydrostatic shallow water model (SW); the HE-NHP model; and the HR-NHP model. For the computational simulation, the initial condition is a constant level of 0.4 m at rest, which is also set as H_0. The outlet is considered closed, as the water never reaches the top of the beach. At the inlet boundary condition, imposed at the position of probe 1, the time variation of water level registered during the experiment is imposed. However, as the time interval of experimental data are not the same as the time steps of the model -governed by the CFL condition in Eqs. (40) and (54), a linear interpolation of the inlet data is done dynamically as the simulation evolves. The NH pressure and vertical velocity are considered null at inlet point. The bed is assumed frictionless.

In this work, four different analysis are carried out through the simulations: an analysis of the non-hydrostatic effects comparing the HE-NHP and the SW model; a second analysis of the mesh size effects simulated with all the presented models over four different meshes with 2000, 4000, 8000 and 16,000 cells; and a third analysis, in which the HR-NHP model is used computing the finest grid with three different α values (see Eq. (15d)), $\alpha = (3, 5, 10)$, to asses the behaviour of the model and its sensitivity to α; and, finally, a frequency analysis is carried out through the *Fast Fourier Transform* (FFT) to compare the simulations and the experimental data.

In Fig. 12 the spatial distributions of water level are shown at $t = 20$ s as simulated with the hydrostatic (SW) and the HE-NHP models. The distribution of vertical velocity, w, and the non-hydrostatic pressure, p_{nh} from the HE-NHP can be observed (as both variables are neglected in the SW model). The presence of these distributions modifies the horizontal velocity field and provokes differences on the water level of the NHP model with respect to the SW results. Simulations with both models have been carried out with CFL = 0.95.

The SW model accounts only for the non-linear effects of the system, that tend to provoke wave steepening generating very discontinuous wave fronts, as seen in the green line in Fig. 12. On the other hand, this tendency is compensated by the dispersive effects when simulating with a NHP model so that the sharp shape of the waves becomes smoother. However,

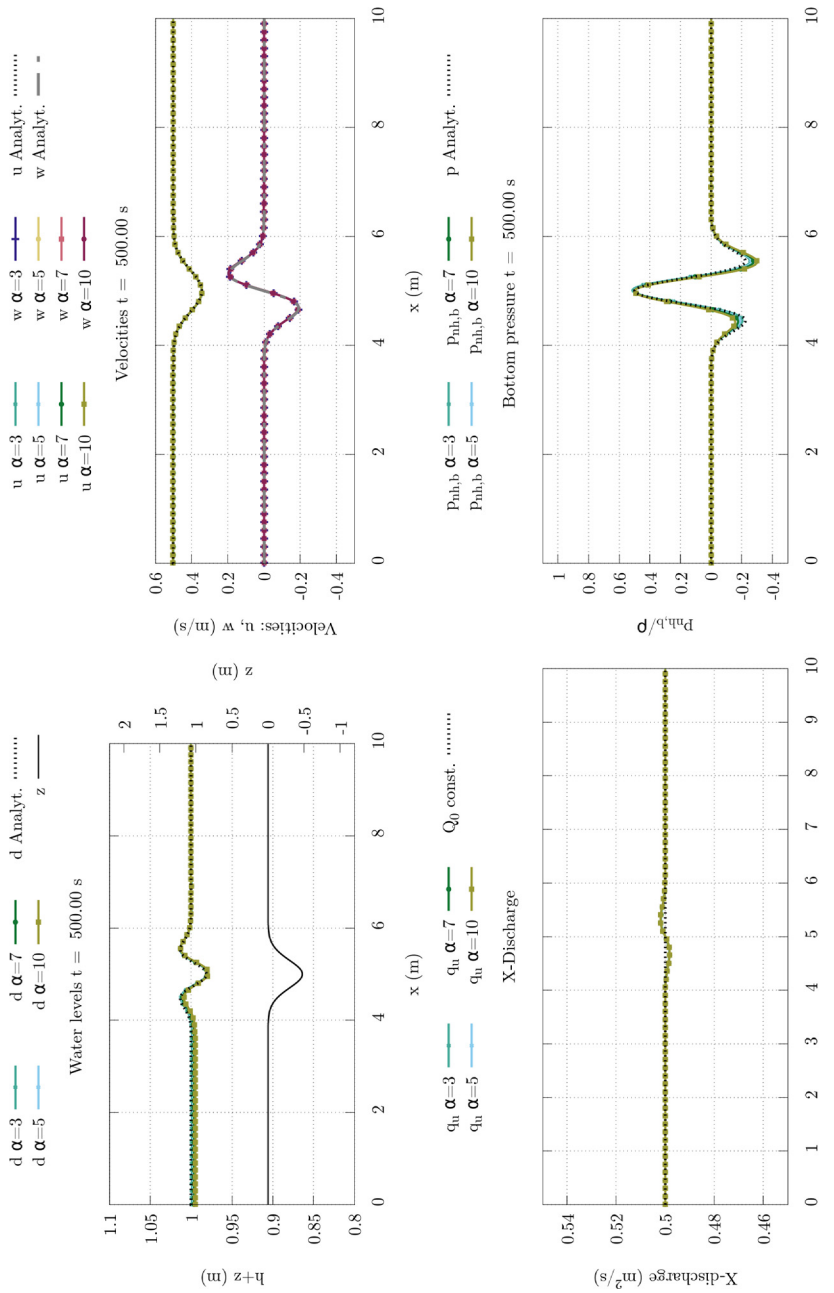

Fig. 9. Variables distribution in the numerical solution for steady state case 1 with HR-NHP.

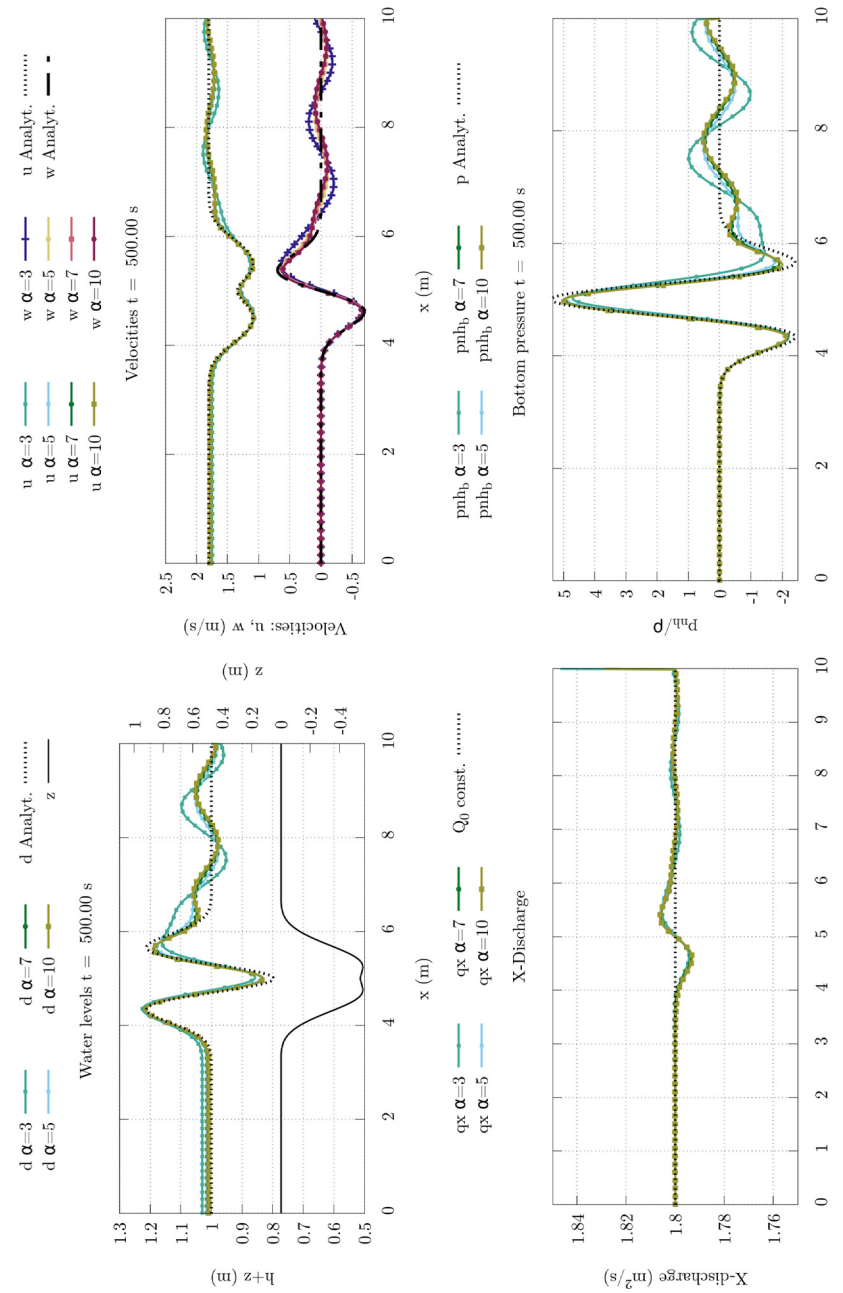

Fig. 10. Variables distribution in the numerical solution for steady state case 2 with HR-NHP.

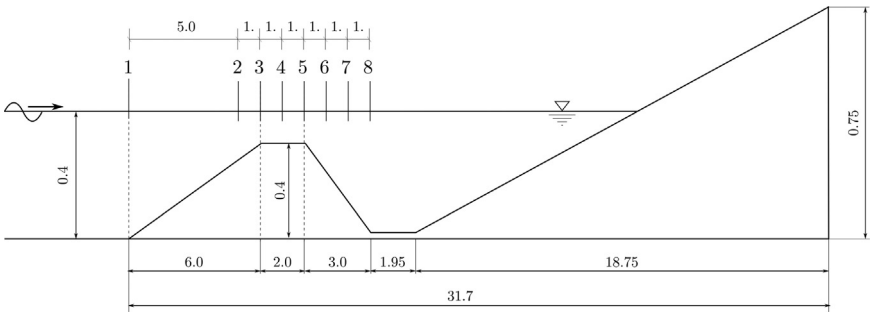

Fig. 11. Sketch of experimental setup and location of waves in flume. All dimensions in meters.

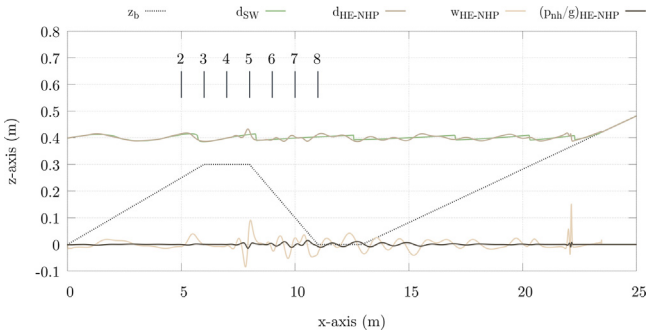

Fig. 12. Spatial distribution of water level, d, for SW and HE-NHP models and vertical velocity, w, and NH pressure (p_{nh}) for NH-NHP model at time = 20 s.

the figure shows how the bottom bar generates more harmonics that only the NHP model is able to reproduce (registered in probes from 2 to 4), and how this effect is even more obvious during the wave release in the deeper region (probes from 5 to 8).

In Figs. 13 and 14, the temporal variation of the perturbation, η, as computed from both models are compared with experimental data. Although experimental data are available during 100 s, the periodic nature of the experiment makes all the results redundant and only waves are plotted from 20 s -to ensure developed flow- to 30 s. This time is enough to see that, as long waves travel upslope, the first probes register the loosing of the waves' vertical symmetry presenting a saw-toothed shape. This effect is well reproduced by both, the SW and the NHP model. However, an increase of wave amplitude is observed in the wave crest due to an energy transmission that the SW model is not able to reproduce. From probe 3 to 5, the waves travel along a flat extension, which might be considered non-dispersive. In this region, there is an energy transmission from the main waves to higher harmonics that only the NHP model is able to reproduce, while the SW model keeps a unique and sharp wave. These higher harmonics travel at almost the same celerity as the primary waves. They are usually called dispersive tail waves and are commonly reported in soliton propagation. As the group of waves moves into the deeper region (probes from 6 to 8), these tail waves decompose into more waves of smaller amplitudes due to the downslope. The NHP system perfectly reproduces this phenomenon, unlike the SW model.

However, it is important to remark the importance of spatial discretization and mesh convergence reached by both models. In Figs. 13 and 14, while the SW system presents almost the same results with the coarsest (2000 cells) and finest meshes (16,000 cells), the HE-NHP model shows the necessity of a very fine discretization to reproduce properly the wave amplitude. This might highlight the suitability of using higher order numerical schemes for solving these equations.

The same test case has been carried out with the HR-NHP model over several meshes with the same discretization: 2000, 4000, 8000 and 16,000 cells. The results for the 4 meshes compared with experimental data can be seen in Figs. 15 and 16. To make use of this model, it is necessary to set a value for the α parameter (see Eq. (15d), where $k = \alpha\sqrt{gH_0}$). For the mesh convergence analysis, this α value is set to 3, as it is a typical used value [32]. Unlike when using the explicit source term shown in Eq. (51), $\mathbf{S}_{nh}^{\exp}$, where low CFL numbers as 0.1 are required, the CFL is set to 0.95 in these simulations using an implicit modelization of source term, $\mathbf{S}_{nh}^{imp}$. Although the simulations with $\alpha = 3$ are the ones that present a dispersive behaviour more distant from that of the HE-NHP model, as can be read in the literature [32], the results it provides are good enough and it has been used for its speed to perform the discretization sensitivity analysis. It is important to note that for 2000 cells the model still returns different results, which then converge to the same with finer meshes. Again, the suitability of a higher order model is reflected by this type of results which, although they are in good agreement with the experimental measurements, require a high number of computational elements.

Additionally, a comparison of the HE-NHP and HR-NHP models with different α is carried out for the finest grid (16,000 cells). The results for all the probes are plotted in Figs. 17 and 18. As reported by Escalante et al. [32], the results in terms

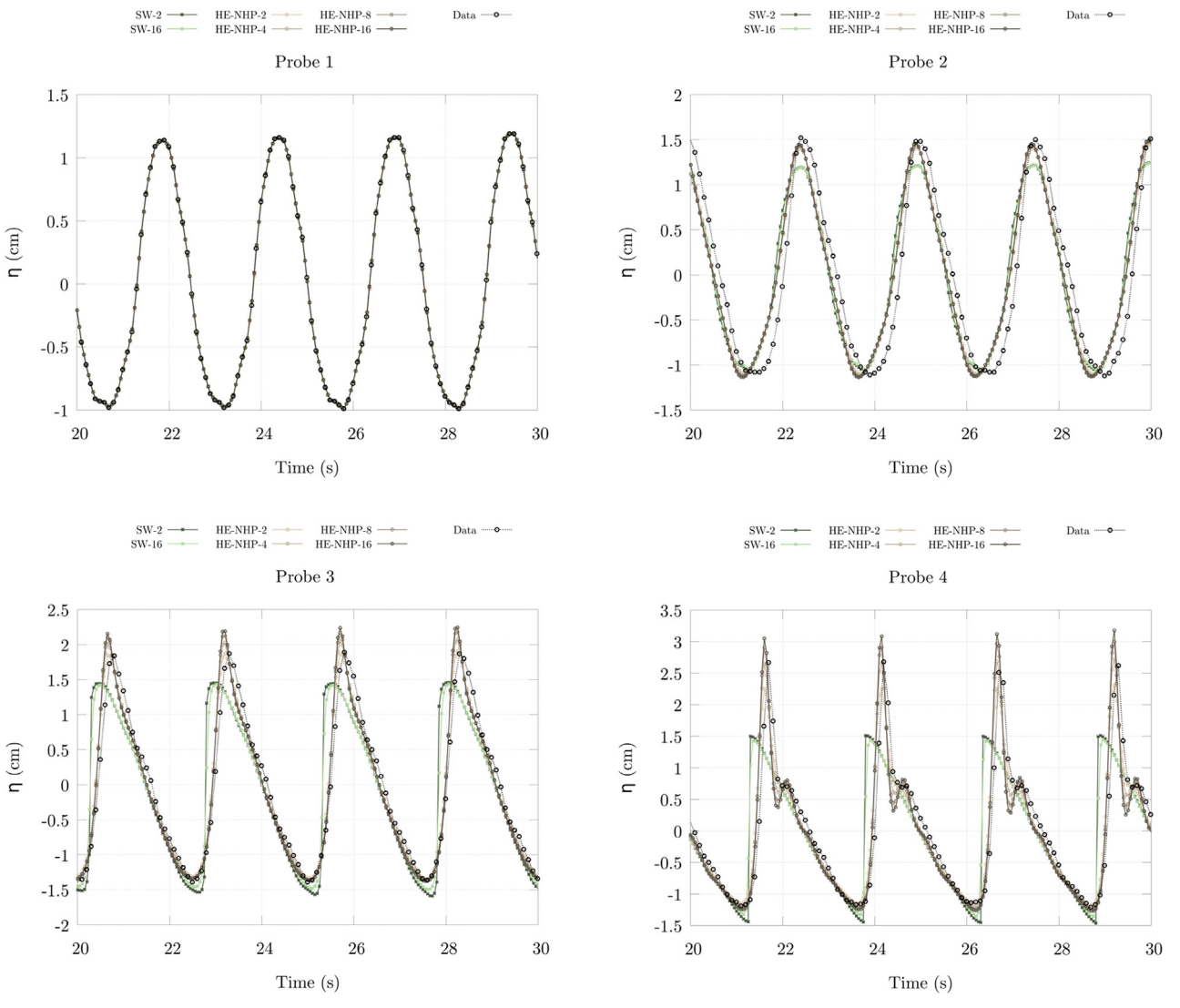

Fig. 13. Time evolution of surface perturbation, η, in cm, for the probes in the shallow area simulated with SW and HE-NHP models, with several computational meshes of 2000, 4000, 8000 and 16,000 cells.

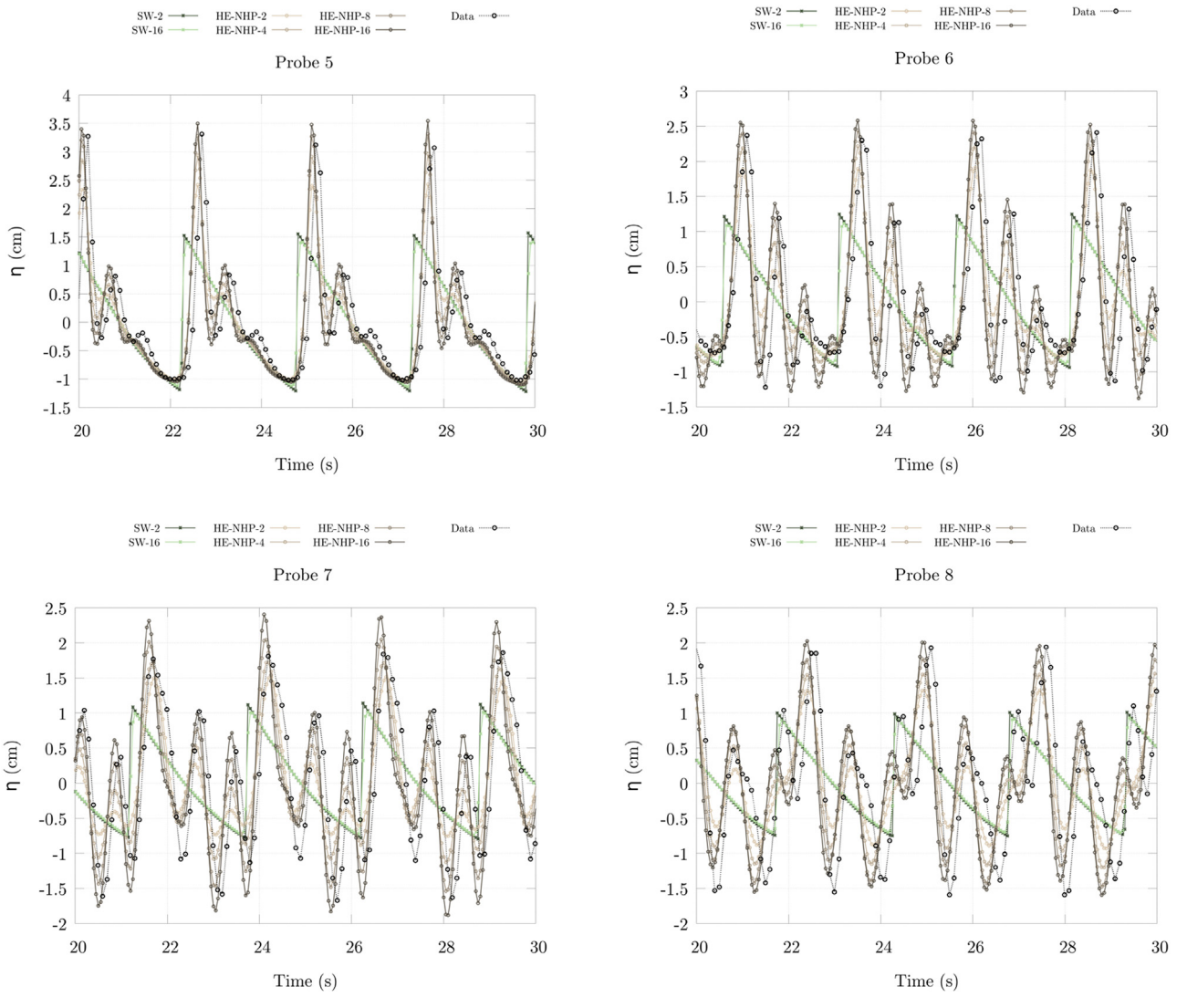

Fig. 14. Time evolution of surface perturbation, η, in cm, for the probes deeper region simulated with SW and HE-NHP models, with several computational meshes of 2000, 4000, 8000 and 16,000 cells.

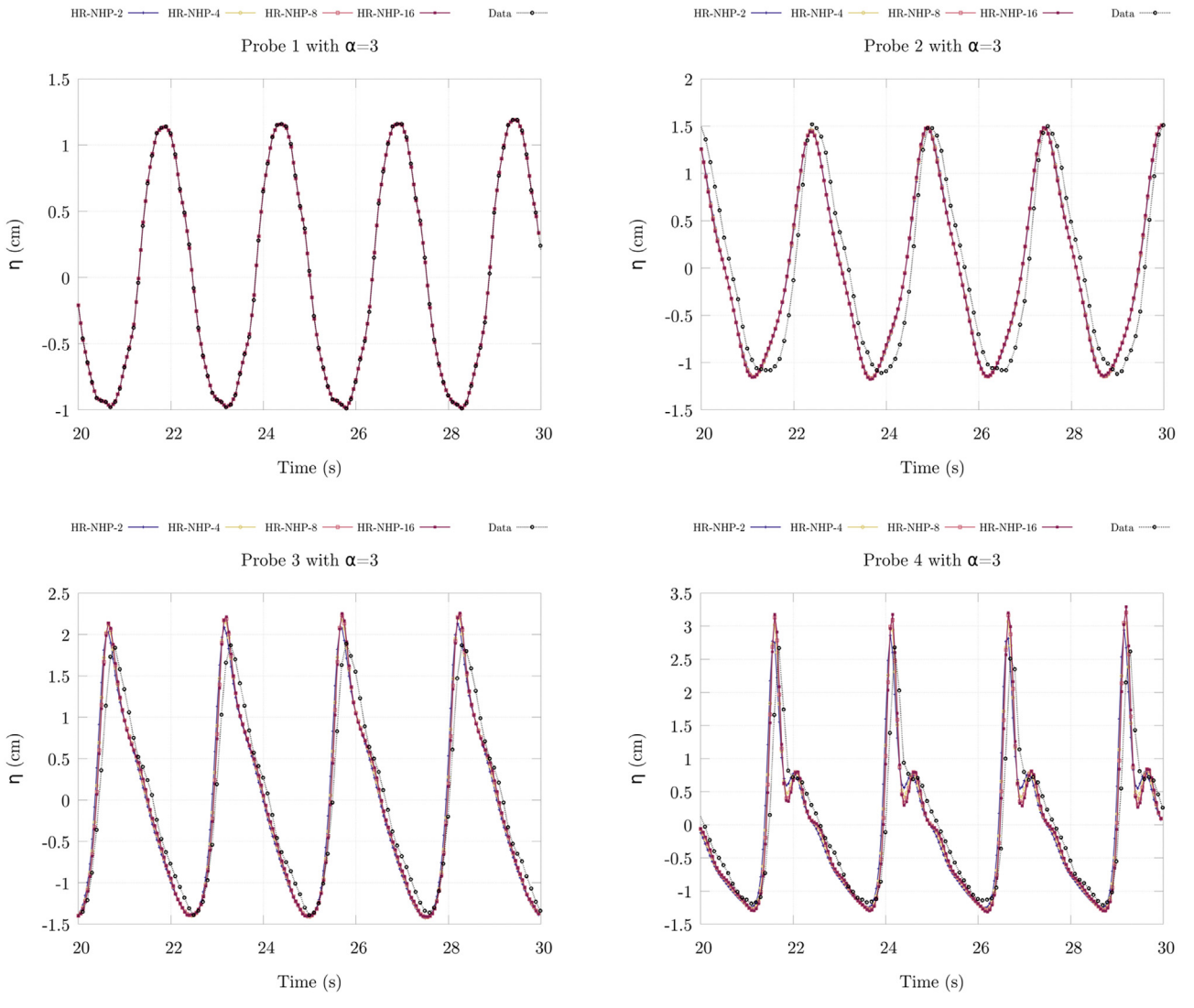

Fig. 15. Time evolution of surface perturbation, η, in cm, for the probes in the shallow area simulated with HR-NHP model, with several computational meshes of 2000, 4000, 8000 and 16,000 cells.

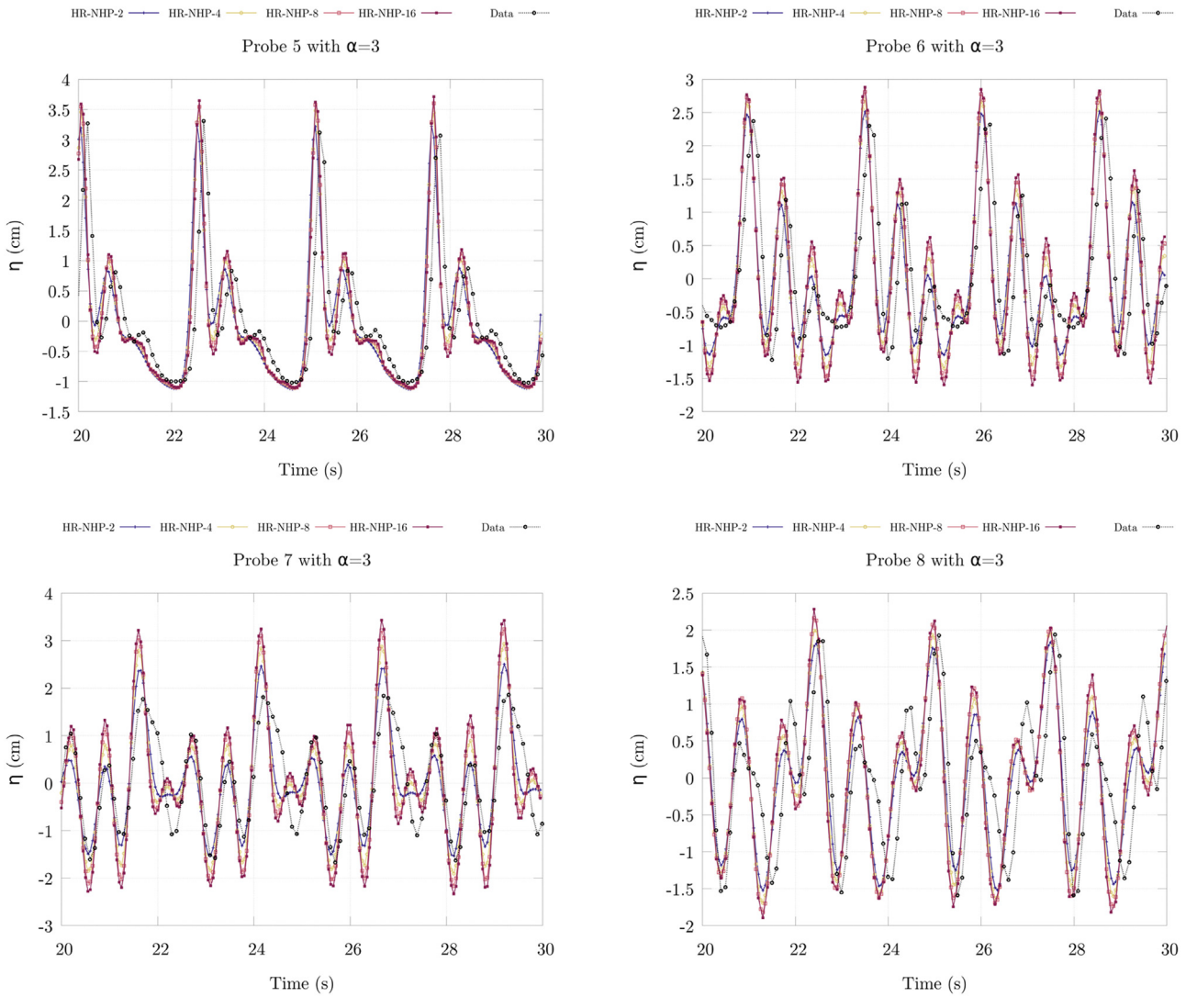

Fig. 16. Time evolution of surface perturbation, η, in cm, for the probes deeper region simulated with HR-NHP model, with several computational meshes of 2000, 4000, 8000 and 16,000 cells.

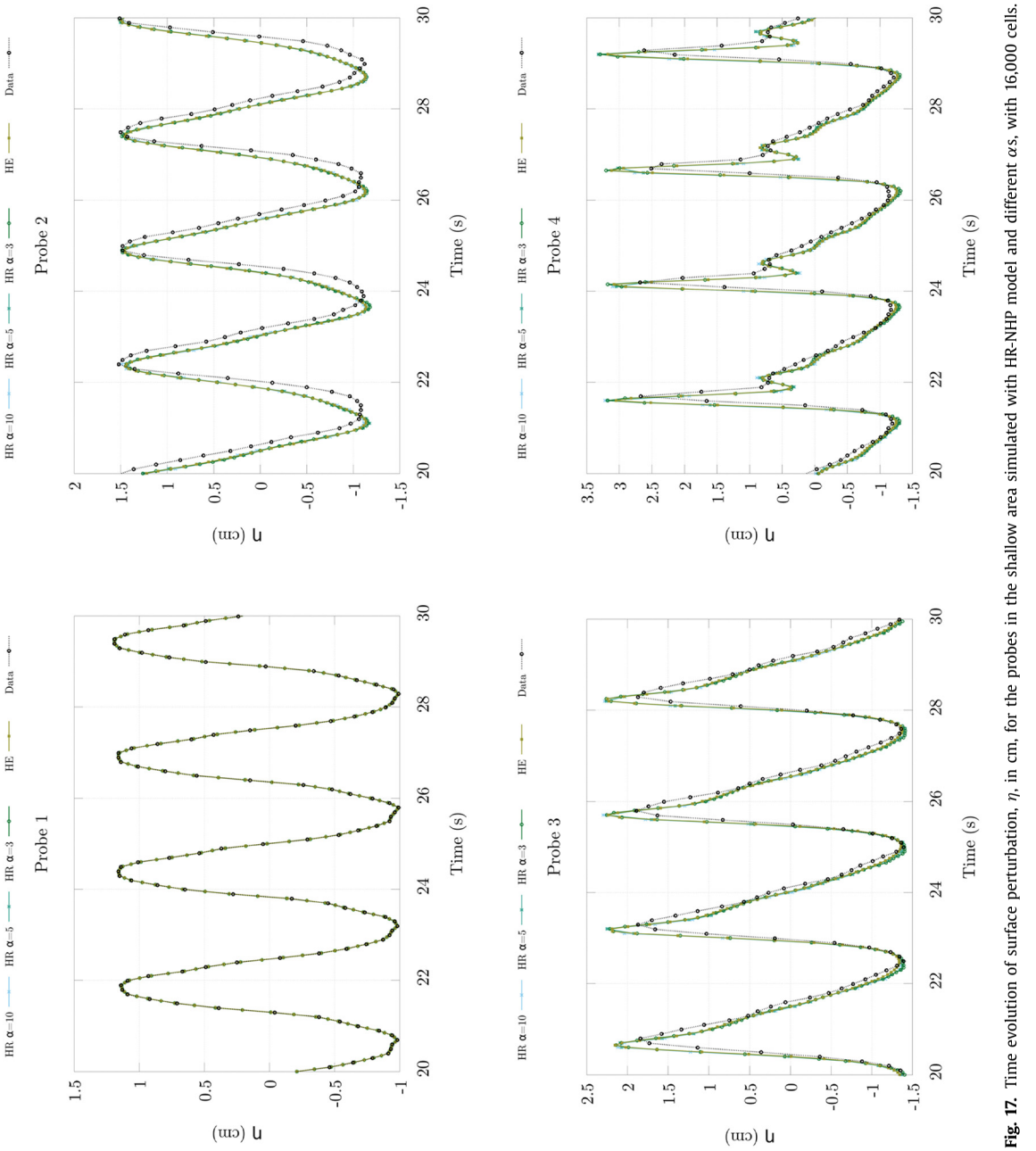

Fig. 17. Time evolution of surface perturbation, η, in cm, for the probes in the shallow area simulated with HR-NHP model and different αs, with 16,000 cells.

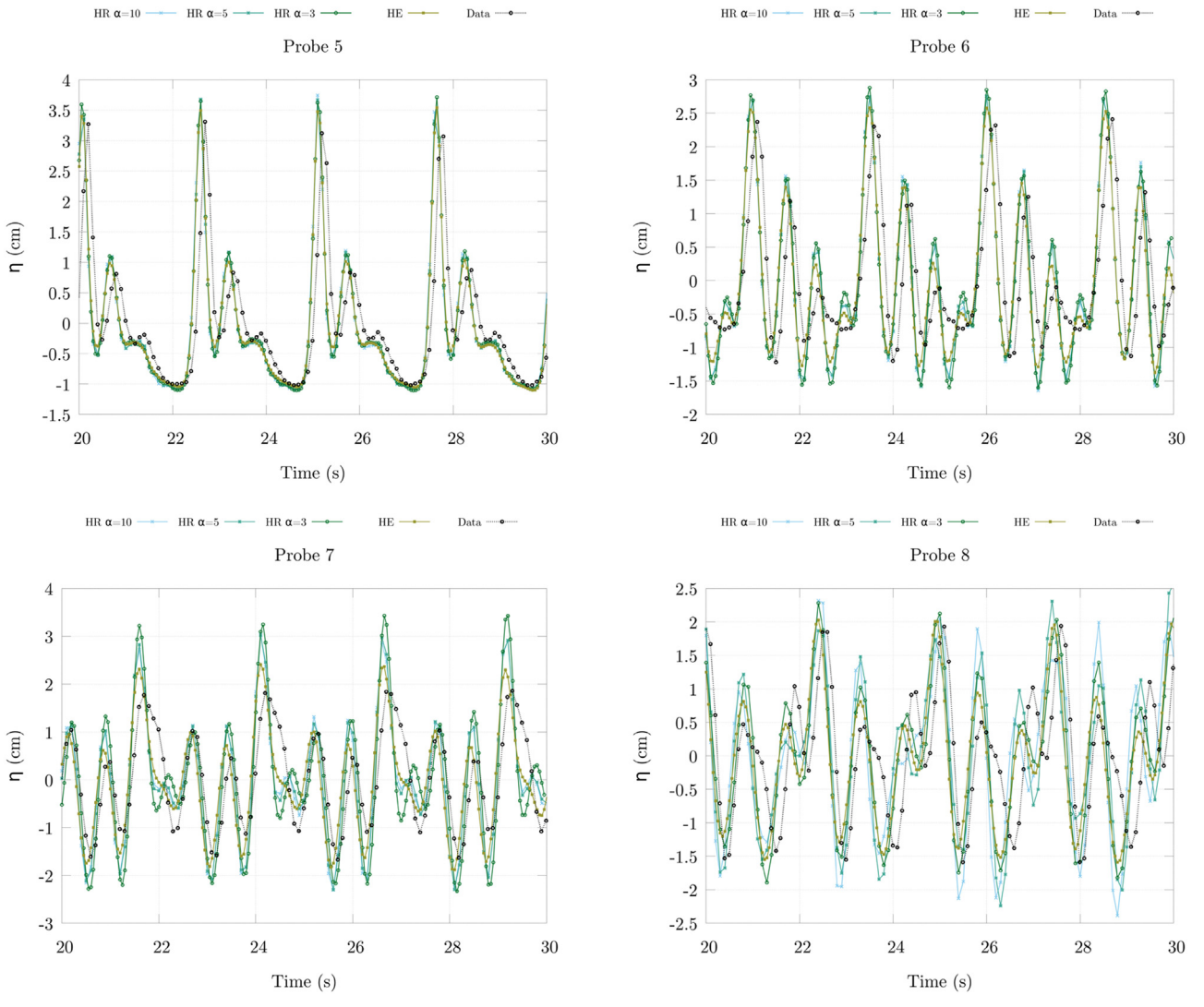

Fig. 18. Time evolution of surface perturbation, η, in cm, for the probes deeper region simulated with HR-NHP model and different αs, with 16,000 cells.

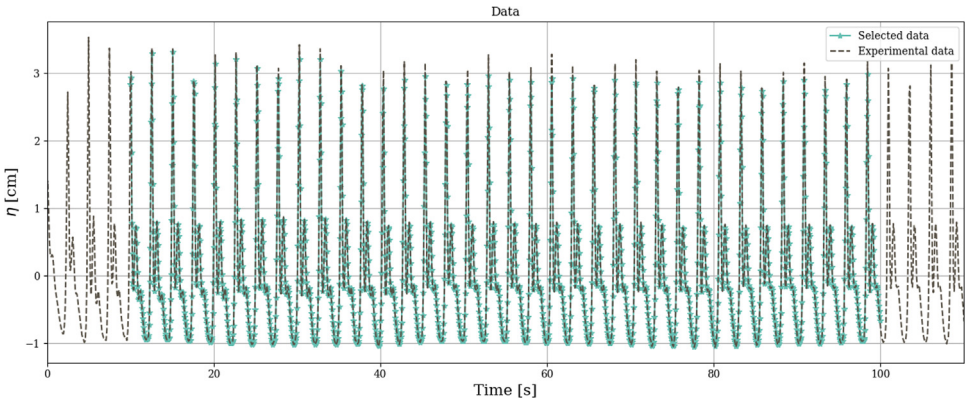

Fig. 19. Experimental data and selected window to perform the FFT in the whole temporal domain.

Table 3
Computational times for the Beji case with different models over a mesh with 16,000 cells.

Model	Time	Avg. Δ t
HR ($\alpha = 3$)	13 m 43.5 s	0.000313
HR ($\alpha = 5$)	22 m 49 s	0.000195
HR ($\alpha = 10$)	43 m 42.6 s	9.9192e−05
HE	2 m 44 s	0.000959

of phase velocities depend on the celerity k and the wavenumber. Therefore, the effect of k depends on the simulated case. However, the results are quite similar until probe 6, no matter the value of α. The high frequency waves generated in the downslope area of the domain present more different amplitudes depending on α, generating even more waves than the measured for lower values of α, which are more distant from HE-NHP in dispersive terms. In the same figures, the results of the HE-NHP are plotted to compare. It is seen how the higher α is, the more similar are the results to those provided by the HE-NHP model.

Finally, a frequency analysis is done applying the FFT to the computational and experimental data. In this case, the Python library *fft* from SciPy is applied to get the main harmonics generated by the models and present in the measured data. All the models are run with a mesh containing 8,000 computational cells. Fig. 19 shows the available time series of experimental and computational data and the selected window to perform the FFT analysis. Boundaries are not included to avoid noise and problems with the algorithm. The sampling rate is 20 Hz and the analysis is performed in a time interval between 10 s and 100 s. All the analysis is performed in probe 5, for instance.

In Fig. 20(a) the frequency analysis of the experimental data and computational results provided by a hydrostatic SW model and the NHP models are displayed. All the frequencies are plotted to show the captured harmonics in 20(a), together with a zoom of the fourth harmonic 20(b). In Fig. 21, the harmonics amplitude for each frequency and all the models are plotted in a bar diagram.

In order to analyse the results, it must be noted that the harmonics of a signal are multiples of the main frequency, which is dominated by the boundary condition. Therefore, all the models capture not only the frequency of the first harmonic, which is generated by the inlet, but also that of the secondary harmonics as multiple of the main one. Concerning the comparison between hydrostatic and non-hydrostatic effects, Fig. 20(a) shows that both SW and HE-NHP models capture the frequencies of the experimental data. However, Fig. 20(b) shows that the amplitudes are not well captured by the SW model, while the HE-NHP system reproduces them properly. This is because the FFT of a saw-tooth signal, as the one of the SW model, is always formed by a group of sinusoidal signals whose amplitude decreases exponentially. Therefore, although SW frequencies match the experimental data, only the first harmonic is well captured in terms of amplitude. However, in the HE-NHP system, secondary harmonics captured by the FFT show a good agreement with the experimental data. Besides that, shock waves provoke high frequency noise present on the SW analysis that must not be taken into account. Finally, the results of the HR-NHP model depend on the selected α parameter, although main frequencies are also properly captured. It is also worth noting that the HR-NHP provides more noise -intermediate frequency waves- than the HE-NHP model.

Finally, in Tables 3 and 4 computational CPU times are collected for the different meshes and models. In particular, Table 3 shows that, for the same refinement, the computational times are very different between both models due to the time step size computation, which is different in both models and much smaller in HR-NHP cases. Additionally, it shows how Δt decreases when artificial celerity, k, (affected by α) increases.

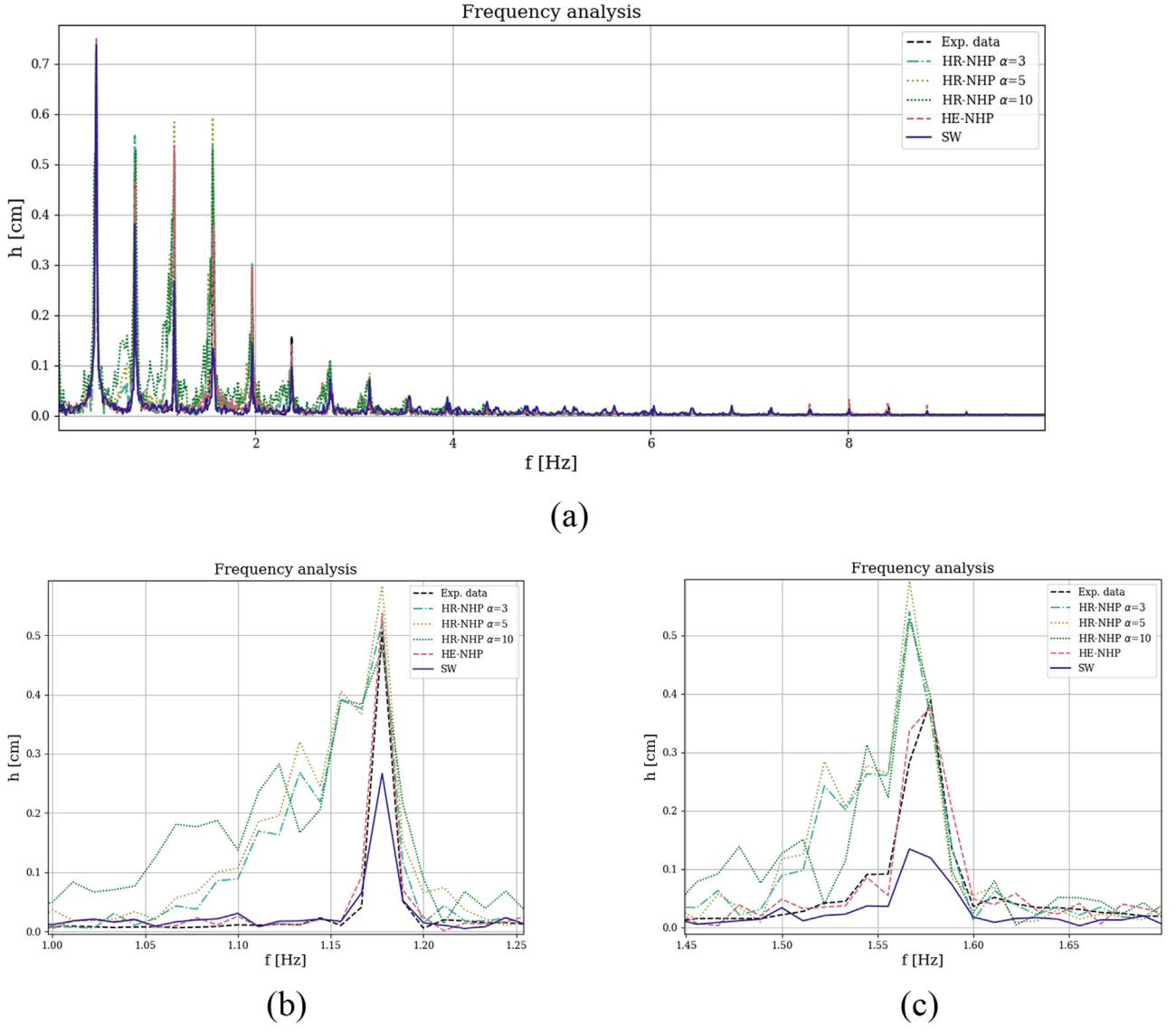

Fig. 20. Frequency analysis obtained by means of the FFT applied to experimental data and computational data provided by a hydrostatic SW model and by all the NHP models (a) and a zoom of the third (b) and fourth (c) harmonic.

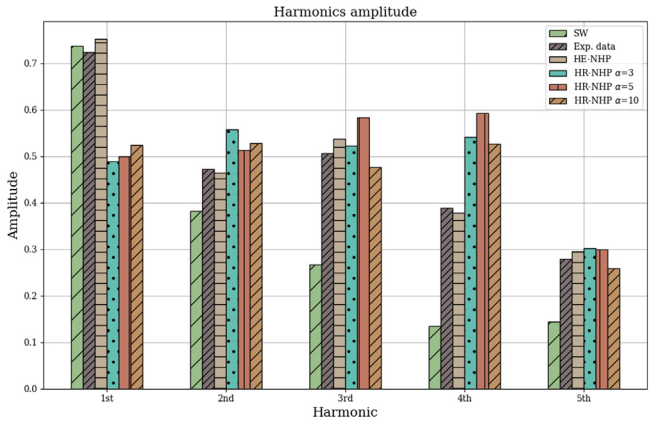

Fig. 21. Amplitude comparison for each harmonic and model.

Table 4
Computational times for the Beji case with different meshes comparing HE-NHP model and HR-NHP model with $\alpha = 3$.

N cells	HR ($\alpha = 3$)	HE
16,000	13 m 43.5 s	2 m 44 s
2000	13.82 s	2.7 s

7. Conclusions

This paper brings together several research efforts that have been focused on different aspects related to depth averaged non-hydrostatic pressure models in free surface flow applications. Firstly, a way to solve the hyperbolic-elliptic system for non-hydrostatic pressure models (HE-NHP) [21] with a first-order Roe's solver for the hyperbolic part, commonly used in shallow water hydrostatic models, has been presented. It has been shown that such scheme combines well with an implicit numerical model that solves the Poisson equation associated to the non-hydrostatic pressure, allowing to extend, in a simple way, a robust shallow water model with all its previous numerical controls to a non-hydrostatic pressure one. In addition, it has been shown that a numerical first-order model can provide good results for this type of dispersive problems.

Secondly, considering the effort involved in solving implicitly one part of the system of equations, an upwind Roe-type scheme has been applied to a system of equations that governs the same phenomenon but being purely hyperbolic (HR-NHP). For this purpose, a new Roe scheme has been developed and new averaged values have been obtained for the non-hydrostatic system involving w and p_{nh}. The results show how the Roe solver works well solving explicitly the fully coupled equations of the hyperbolic relaxation system, specially if a local implicit formulation of non-hydrostatic source terms is applied.

For both models, their dispersive performance has been evaluated with test cases. In the steady flow case, both models show a dispersive behaviour typical for non-hydrostatic models, which generate downstream wave trains in the presence of discontinuities. In turn, both models tend to correctly solve the discontinuous part of the stationary case. However, the HR-NHP model shows a slight dependence of the results on the compressibility α parameter, which becomes more noticeable the more dispersive the case is.

On the other hand, both models have been applied to a laboratory case in order to compare with experimental data and both models adequately capture the generation of high-frequency waves that occur in cases of wave propagation with background variation, contrary to the hydrostatic model. In addition, in order to analyze the dispersive behaviour of both non-hydrostatic models and the shallow water model, a frequency analysis has been performed through FFT. The results have shown that, although the boundary condition governs the first harmonic and, therefore, all models capture it adequately, the amplitude of the secondary harmonics is only captured when using a non-hydrostatic pressure model such as HE-NHP. On the other hand, the HR-NHP model also captures properly the main harmonics of the test case, but introduces more noise generating intermediate frequency waves not present on measurements. Additionally, this test has shown the importance of the α parameter, that controls the dispersive behaviour of the HR-NHP model, providing the results more similar to the experimental data for higher values of α. However, this model always needs to find a balance between the proper dispersive behaviour and the efficiency, which decreases as α increases.

Regarding the computational aspect, although both models show good results, the computational time needed by the HR-NHP is higher than that invested by the HE-NHP, despite the fact that the latter has to solve implicitly an equation every

time step, while the former solves the whole system coupled and explicitly. The reason is the stability constraint presented by the HR-NHP model, that introduces α in the time step size with the CFL condition. At this point, it is important to remark that the implicit formulation of the source term $\mathbf{S}_{nh}$ allows the use of higher CFL numbers. However, when this term is modelled explicitly, the time step size constrains are even bigger and the model results less efficient. Additionally, in this model, the time step size is governed not only by an external parameter, k, but also by an average water depth, H_0, that also has to be chosen externally and that is not always the most suitable over irregular topography. On the other hand, it is important to note that the priority of these conclusions may be different when these models are extended to 2D for larger realistic cases. The extension to 2D increases the complexity of the HE-NHP, which could not be solved with the Thomas Algorithm, while the extension of the HR-NHP is more direct. In addition, it is important to mention that when simulation realistic cases parallelization becomes necessary. In that case, the implicit model would present a clear bottleneck, while the purely explicit model could be fully parallelized. Finally, since it has been shown that in some cases the use of higher order schemes may be necessary, it is important to note that the design of higher order methods is much simpler within the framework of the HR-NHP model than within the PCM used to solve the HE-NHP system. Therefore, the suitability of one system or another depends on the type of case to be solved, the computational needs and the mathematical tools available.

Acknowledgements

Hydronia Europe S.L. has funded part of this research by means of a Industrial Doctorate Research Grant DIN2018-010036. Additionally, this work is also part of the PGC2018-094341-B-I00 research project funded by the Ministry of Science and Innovation/FEDER.

Appendix A. Artificial compressibility for the evolution of non-hydrostatic pressure

The Artificial Compressibility Method (ACM) was first introduced by Chorin [33] to solve incompressible viscous flows. The principle of the method lies in the introduction of an artificial compressibility that allows to transform the fundamental equation of fluid mechanics into a total pressure evolution equation. Then, in this case, the total pressure is split into its hydrostatic and non-hydrostatic part getting an equation only for the non-hydrostatic pressure, p_{nh}, which is one of the variables of the HR-NHP system.

The fundamental continuity equation of a viscous flow is

$$\frac{\partial \rho}{\partial t} + \vec{\nabla} \cdot (\rho \vec{\mathbf{v}}) = 0, \tag{A.1}$$

where $\vec{\mathbf{v}}$ is the velocity vector, that will be assumed $\vec{\mathbf{v}} = (u, w)$ in this case. Developing

$$\frac{\partial \rho}{\partial t} + \rho \vec{\nabla} \cdot \vec{\mathbf{v}} + \vec{\mathbf{v}} \cdot \vec{\nabla} \rho = 0. \tag{A.2}$$

Assuming that $\rho = \rho(p)$ being p the total pressure, it can be written

$$\frac{\partial \rho}{\partial p} \frac{\partial p}{\partial t} + \vec{\mathbf{v}} \frac{\partial \rho}{\partial p} \vec{\nabla} p + \rho \vec{\nabla} \vec{\mathbf{v}} = 0, \tag{A.3}$$

or

$$\frac{1}{\rho} \frac{\partial \rho}{\partial p} \left(\frac{\partial p}{\partial t} + \vec{\mathbf{v}} \vec{\nabla} p \right) + \vec{\nabla} \vec{\mathbf{v}} = 0, \tag{A.4}$$

Defining

$$\frac{1}{\rho} \frac{\partial \rho}{\partial p} = \frac{1}{k^2} \tag{A.5}$$

where k can be denominated as the artificial sound speed parameter. Its form depends on the model and is explained in Eq. (17) of the main text. With this definition, the final equation reads

$$\frac{\partial p}{\partial t} + \vec{\mathbf{v}} \vec{\nabla} p + k^2 \left(\vec{\nabla} \vec{\mathbf{v}} \right) = 0, \tag{A.6}$$

This new equation with k multiplying the divergence of the velocity provides the evolution of the total pressure. However, for the non-hydrostatic models that solve intrinsically the hydrostatic part, a specific evolution equation for the p_{nh} results more interesting. Applying the basis of the model: $p = g(h_s - z) + p_{nh}$, Eq. (A.5) turns into

$$\frac{\partial}{\partial t} (g(h_s - z) + p_{nh}) + \vec{\mathbf{v}} \cdot \vec{\nabla} (g(h_s - z)) + \vec{\mathbf{v}} \cdot \vec{\nabla} p_{nh} + k^2 \vec{\nabla} \cdot \vec{\mathbf{v}} = 0 \tag{A.7}$$

Developing

$$g \left(\frac{\partial h_s}{\partial t} + u_s \frac{\partial h_s}{\partial x} - w_s \right) + \frac{\partial p_{nh}}{\partial t} + \vec{\mathbf{v}} \cdot \vec{\nabla} p_{nh} + k^2 \vec{\nabla} \cdot \vec{\mathbf{v}} = 0 \tag{A.8}$$

where u_s and w_s refer to the velocity components at the free surface, so that the terms inside the brackets conform the surface boundary condition, that can be cancelled. Thus, the final equation reads

$$\frac{\partial p_{nh}}{\partial t} + \vec{\mathbf{v}} \cdot \vec{\nabla} p_{nh} + k^2 \vec{\nabla} \cdot \vec{\mathbf{v}} = 0 \tag{A.9}$$

Finally, this equation must be depth integrated to be used in the model with the rest of averaged variables of the system.

$$\int_{z_b}^{h_s} \frac{\partial p_{nh}}{\partial t} dz + \int_{z_b}^{h_s} \vec{\mathbf{v}} \cdot \vec{\nabla} p_{nh} dz + \int_{z_b}^{h_s} k^2 \vec{\nabla} \cdot \vec{\mathbf{v}} dz = 0 \tag{A.10}$$

An averaged non-hydrostatic pressure is defined as

$$\bar{p}_{nh} = \frac{1}{h} \int_{z_b}^{h_s} p_{nh} dz \tag{A.11}$$

Reordering and extracting common factors

$$\begin{aligned} &\frac{\partial (h\bar{p}_{nh})}{\partial t} + \frac{\partial (h\bar{u}\bar{p}_{nh})}{\partial x} - p_{nh,s}\left(\frac{\partial h_s}{\partial t} + u_s \frac{\partial h_s}{\partial x} - w_s\right) + p_{nh,b}\left(\frac{\partial z_b}{\partial t} + u_b \frac{\partial z_b}{\partial x} - w_b\right) \\ &\quad + k^2\left(\frac{\partial (h\bar{u})}{\partial x} - u_s \frac{\partial h_s}{\partial x} + u_b \frac{\partial z_b}{\partial x} + w_s - w_b\right) = 0 \end{aligned}$$

where subindexes s and b refer to surface and bottom, respectively. During the whole derivation of this model, the vertical profiles of velocity are assumed to be

$$u(z) = \text{const.} = \bar{u}, \quad \text{and} \quad w(z) = \frac{w_s - w_b}{h} + w_b \rightarrow \bar{w} = \frac{w_s + w_b}{2} \tag{A.12}$$

Thus, substituting the final depth-averaged equation for the non-hydrostatic pressure evolution reads

$$\frac{\partial (h\bar{p}_{nh})}{\partial t} + \frac{\partial (h\bar{u}\bar{p}_{nh})}{\partial x} + k^2\left(\frac{\partial (h\bar{u})}{\partial x} - \bar{u}\frac{\partial h}{\partial x} + 2\bar{w} - 2\bar{u}\frac{\partial z_b}{\partial x}\right) = 0 \tag{A.13}$$

or:

$$\frac{\partial (h\bar{p}_{nh})}{\partial t} + \frac{\partial (h\bar{u}\bar{p}_{nh})}{\partial x} + k^2\left(\frac{\partial (h\bar{u})}{\partial x} + 2\bar{w} - \bar{u}\frac{\partial (h + 2z_b)}{\partial x}\right) = 0 \tag{A.14}$$

For the sake of clarity, bars are removed from equation in the main text.

Appendix B. Details of numerical schemes

B1. Coefficients of the implicit scheme for HE-NHP model

As the DIIC is discretized to be solved in cell edges of the computational mesh, all the derivatives of the equations are discretized between cell i and $i+1$ for wall $i+1/2$. Therefore, the coefficients in Eq. (47) are of the form:

$$\begin{aligned} A_{i+1/2} &= \left(\frac{\phi_i}{2} - 2h_i\right)\left(\phi_{i+1/2} - 2h_{i+1/2}\right) \\ B_{i+1/2} &= 16\Delta x^2 + \phi_{i+1/2}(\phi_i/2 + \phi_{i+1}/2 + 2h_{i+1} - 1 - 2h_{i+1}) \\ &\quad + 2h_{i+1/2}\left(\phi_i/2 - \phi_{i+1}/2 + 4h_{i+1/2}\right) \\ C_{i+1/2} &= \left(\frac{\phi_{i+1}}{2} - 2h_{i+1}\right)\left(\phi_{i+1/2} - 2h_{i+1/2}\right) \\ D_{i+1/2} &= \frac{4\Delta x^2}{\Delta t}\left[h_{i+1/2}\frac{(hu)_{i+1} - (hu)_i}{\Delta x} - (hu)_{i+1/2}\frac{\phi_{i+1/2}}{\Delta x} + 2h_{i+1/2}w_{i+1/2}\right] \end{aligned} \tag{B.1}$$

where $\phi_{i+1/2} = h_{i+1} + 2z_{i+1} - h_i - 2z_i$.

Note that the formulation using the non-hydrostatic pressure at the bottom, $p_{nh,b}$ (instead of average, p_{nh}), is widely extended [21,28] and, as it can be proved to be $p_{nh,b} = 2p_{nh}$ [21], formulation can vary by a factor of 2. In this case, when bottom pressure is used, $D_{i+1/2}$ must be multiplied by 2, and $\mathcal{Q}(p_{nh})$ and $\mathcal{W}(p_{nh})$ in Eqs. (44) and (45), must be also multiplied by 1/2 [21,28].

B2. Roe averages

B2.1. Roe averages for the hydrostatic part of the HE-NHP system (SWE)

One approach to define an approximate Riemann solution is to replace the nonlinear problem of a system (i.e. the SWE) by some linearized problem defined locally at each cell interface [53]. The Roe solver can be used to perform this linearization. Its basis consists in the transformation of the Jacobian matrix, $\mathbf{J}$, into the Roe's matrix, $\widetilde{\mathbf{J}}$. The definition of the Jacobian matrix is:

$$\mathbf{J} = \frac{\partial \mathbf{F}}{\partial \mathbf{U}}, \tag{B.2}$$

and the Roe's matrix connects the discretization of partial derivatives of fluxes and conserved variables as:

$$\widetilde{\mathbf{J}} = \frac{\delta \mathbf{F}}{\delta \mathbf{U}} \quad \rightarrow \quad \widetilde{\mathbf{J}}\delta\mathbf{U} = \delta\mathbf{F}. \tag{B.3}$$

The whole construction of the Roe's matrix can be seen in LeVeque [53]. Here, the determination of the averaged velocity, $\widetilde{u}$, and celerity, $\widetilde{c}$, is developed. Given the homogeneous SWE:

$$\frac{\partial \mathbf{U}}{\partial t} + \frac{\partial \mathbf{F}}{\partial x} = 0 \quad \rightarrow \quad \frac{\partial \mathbf{U}}{\partial t} + \mathbf{J}\frac{\partial \mathbf{U}}{\partial x} = 0 \tag{B.4}$$

where conserved variables, $\mathbf{U}$, and fluxes, $\mathbf{F}$, are

$$\mathbf{U} = \begin{pmatrix} h \\ hu \end{pmatrix}; \quad \mathbf{F} = \begin{pmatrix} hu \\ hu^2 + \frac{1}{2}gh^2 \end{pmatrix}; \tag{B.5}$$

the approximated Jacobian matrix, $\widetilde{\mathbf{J}}$ is

$$\widetilde{\mathbf{J}} = \begin{pmatrix} 1 & 0 \\ g\widetilde{h} - \widetilde{u}^2 & 2\widetilde{u} \end{pmatrix}. \tag{B.6}$$

The linearized water depth is assumed as a simple average: $\widetilde{h} = 1/2(h_L + h_R)$, as any restriction on its formulation can be extracted from the first component of the system.

Then, when the definition (B.3) is applied for the second component of the system, the following expression can be written:

$$(\widetilde{c}^2 - \widetilde{u}^2)\delta h + 2\widetilde{u}\delta q = \delta\left(\frac{q^2}{h} + \frac{1}{2}gh^2\right) \tag{B.7}$$

Developing

$$\widetilde{c}^2\delta h - \widetilde{u}^2\delta h + 2\widetilde{u}\delta q = \delta\left(\frac{q^2}{h}\right) + \delta\left(\frac{1}{2}gh^2\right) \tag{B.8}$$

the first and last term of the equation give rise to the celerity definition:

$$\widetilde{c}^2\delta h = \delta\left(\frac{1}{2}gh^2\right) \quad \rightarrow \quad \widetilde{c}^2\delta h = \frac{1}{2}g\delta h^2 \quad \rightarrow \tag{B.9}$$

$$\rightarrow \widetilde{c}^2\delta h = \frac{1}{2}g2\widetilde{h}\delta h \quad \rightarrow \quad \widetilde{c}^2\cancel{\delta h} = \frac{1}{\cancel{2}}g\cancel{2}\widetilde{h}\cancel{\delta h} \quad \rightarrow \tag{B.10}$$

$$\widetilde{c} = \sqrt{g\widetilde{h}} \tag{B.11}$$

The remaining part of Eq. (B.12) yields

$$\widetilde{u}^2\delta h - 2\widetilde{u}\delta q + \delta\left(\frac{q^2}{h}\right) = 0 \tag{B.12}$$

that can be solved by means of a second degree equation formula as

$$\widetilde{u} = \frac{\delta q \pm \sqrt{(\delta q)^2 - \delta h\delta(q^2/h)}}{\delta h}; \tag{B.13}$$

Assuming the definition of $\delta = (.)_R - (.)_L$, where subindexes $(.)_L$ and $(.)_R$ refer to values on the left and right side of every cell, respectively, and developing

$$= \frac{\delta q \pm \sqrt{-2h_R u_R h_L u_L + h_R h_L u_L^2 + h_L h_R u_R^2}}{\delta h} = \tag{B.14}$$

Extracting from every term $h_R h_L$

$$= \frac{\delta q \pm \sqrt{h_R h_L(-2u_R u_L + u_L^2 + u_R^2)}}{\delta h} = \tag{B.15}$$

Developing the rest of terms

$$= \frac{h_R u_R - h_L u_L \pm \sqrt{h_R h_L}(u_L - u_R)}{h_R - h_L} = \tag{B.16}$$

Taking the positive sign of the $\pm$, the equation reads

$$= \frac{h_R u_R - h_L u_L + u_L\sqrt{h_R h_L} - u_R\sqrt{h_R h_L}}{(\sqrt{h_R} - \sqrt{h_L})(\sqrt{h_R} + \sqrt{h_L})} = \tag{B.17}$$

And extracting u_L and u_R by pairs, and then $\sqrt{h_R}$ and $\sqrt{h_L}$, it yields

$$= \frac{u_R(h_R - \sqrt{h_R h_L}) + u_L(-h_L\sqrt{h_R h_L})}{(\sqrt{h_R} - \sqrt{h_L})(\sqrt{h_R} + \sqrt{h_L})} = \tag{B.18}$$

$$= \frac{u_R\sqrt{h_R}\cancel{(\sqrt{h_R} - \sqrt{h_L})} + u_L\sqrt{h_L}\cancel{(\sqrt{h_R} - \sqrt{h_L})}}{\cancel{(\sqrt{h_R} - \sqrt{h_L})}(\sqrt{h_R} + \sqrt{h_L})}$$

Therefore, the final averaging for $\widetilde{u}$ reads

$$\widetilde{u} = \frac{u_R\sqrt{h_R} + u_L\sqrt{h_L}}{\sqrt{h_R} + \sqrt{h_L}} \tag{B.19}$$

B2.2. Roe averages for the full HR-NHP system

The same procedure can be applied to the HR-NHP system in order to obtain the linearized values of the problem variables: $\widetilde{c}$, $\widetilde{u}$, $\widetilde{p}_{nh}$ and $\widetilde{w}$. In this case, the Roe matrix is the linearized value of matrix $\widetilde{\mathbf{J}}_{\mathbf{F}}$, and the values inside the matrix must ensure that

$$\widetilde{\mathbf{J}}_{\mathbf{F}}\delta\mathbf{U} = \delta\mathbf{F} \tag{B.20}$$

where:

$$\mathbf{U} = \begin{pmatrix} h \\ q_u \\ q_w \\ q_p \end{pmatrix}, \quad \mathbf{F}(\mathbf{U}) = \begin{pmatrix} q_u \\ \frac{q_u^2}{h} + \frac{1}{2}gh^2 + q_p \\ \frac{q_u q_w}{h} \\ \frac{q_u q_p}{h} + k^2 q_u \end{pmatrix}, \quad \widetilde{\mathbf{J}}_{\mathbf{F}}(\mathbf{U}) = \begin{pmatrix} 0 & 1 & 0 & 0 \\ \widetilde{c}^2 - \widetilde{u}^2 & 2\widetilde{u} & 0 & 1 \\ -\widetilde{u}\widetilde{w} & \widetilde{w} & \widetilde{u} & 0 \\ -\widetilde{u}\,\widetilde{p}_{nh} & \widetilde{p}_{nh} + k^2 & 0 & \widetilde{u} \end{pmatrix}, \tag{B.21}$$

It can be easy demonstrated that the averaged horizontal velocity, $\widetilde{u}$, and the celerity, $\widetilde{c}$, remain the same as in (B.19) for this system when using the first and second equations of (B.20). From the third equation, the vertical velocity is obtained:

$$-\widetilde{u}\widetilde{w}\delta h + \widetilde{w}\delta q + \widetilde{u}\delta q_w = \delta\left(\frac{q q_w}{h}\right), \tag{B.22}$$

Clearing $\widetilde{w}$ leads to

$$\widetilde{w} = \frac{\frac{q q_w}{h} - \widetilde{u}\delta q_w}{\delta q - \widetilde{u}\delta h}. \tag{B.23}$$

Assuming $\delta = (.)_R - (.)_L$, where subindexes $(.)_L$ and $(.)_R$ refer to values on the left and right side of every cell, respectively, and the definition of $\widetilde{u}$ as in (B.19)

$$\widetilde{w} = \frac{h_R u_R w_R - h_L u_L w_L - \frac{u_R\sqrt{h_R} + u_L\sqrt{h_L}}{\sqrt{h_R} + \sqrt{h_L}}(h_R w_R - h_L w_L)}{h_R u_R - h_L u_L - \frac{u_R\sqrt{h_R} + u_L\sqrt{h_L}}{\sqrt{h_R} + \sqrt{h_L}}(h_R - h_L)} \tag{B.24}$$

and developing

$$\widetilde{w} = \frac{\sqrt{h_L}h_R u_R w_R - \sqrt{h_R}h_L u_L w_L + \sqrt{h_L}h_R u_R w_R + \sqrt{h_R}u_R h_L w_L}{\sqrt{h_L}h_R u_R - \sqrt{h_R}h_L u_L + \sqrt{h_R}u_R h_L - \sqrt{h_L}u_L h_R} \tag{B.25}$$

Then, finally:

$$\widetilde{w} = \frac{\sqrt{h_L}h_R w_R + \sqrt{h_R}h_L w_L}{\sqrt{h_L}h_R + \sqrt{h_R}h_L} \tag{B.26}$$

The same procedure can be done with the last equation to find the average value for the non-hydrostatic pressure, $\widetilde{p}_{nh}$. The equation reads:

$$-\widetilde{u}\widetilde{p}_{nh}\delta h + (\widetilde{p}_{nh} + k^2)\delta q + \widetilde{u}\delta q_p = \delta\left(hup_{nh} + k^2 q_u\right), \tag{B.27}$$

Clearing the pressure, the equation writes

$$\widetilde{p}_{nh} = \frac{\delta(hup_{nh}) - \widetilde{u}\delta(q_p)}{\delta(hu) - \widetilde{u}\delta h} \tag{B.28}$$

Assuming $\delta = (.)_R - (.)_L$ and the definition of $\widetilde{u}$ as in (B.19)

$$\widetilde{p}_{nh} = \frac{h_R u_R p_{nh,R} - h_L u_L p_{nh,L} - \frac{u_R\sqrt{h_R}+u_L\sqrt{h_L}}{\sqrt{h_R}+\sqrt{h_L}}\left(h_R p_{nh,R} - h_L p_{nh,L}\right)}{h_R u_R - h_L u_L - \frac{u_R\sqrt{h_R}+u_L\sqrt{h_L}}{\sqrt{h_R}+\sqrt{h_L}}(h_R - h_L)} \tag{B.29}$$

And developing, finally the average pressure reads

$$\widetilde{p}_{nh} = \frac{\sqrt{h_L}h_R p_{nh,R} + \sqrt{h_R}h_L p_{nh,L}}{\sqrt{h_R}h_L + \sqrt{h_L h_R}} \tag{B.30}$$

B3. Wave and source strengths for the Roe-solver system

As explained in the main text, the numerical contributions for the Roe-schemes are computed as

$$\widetilde{\mathcal{A}} = \widetilde{\mathbf{P}}^{-1}\delta\widetilde{\mathbf{U}} \qquad \text{and} \qquad \widetilde{\mathcal{B}} = \widetilde{\mathbf{P}}^{-1}\widetilde{\mathbf{S}}_b. \tag{B.31}$$

where $\widetilde{\mathbf{P}}$ is the eigenvector basis and $\widetilde{\mathbf{S}}_b$ stands for the bed surface source term, all of them linearized at cell edges. Vectors $\widetilde{\mathcal{A}}$ and $\widetilde{\mathcal{B}}$ are obtained and their aspect is

$$\widetilde{\mathcal{A}} = (\widetilde{\alpha}_1, ., \widetilde{\alpha}_m)^T \qquad \text{and} \qquad \widetilde{\mathcal{B}} = (\tilde{\beta}_1, ., \tilde{\beta}_m)^T \tag{B.32}$$

being m the number of waves of the system, which can be 2 or 4 depending on the model.

B3.1. Strengths of the HE-NHP system

The two-wave numerical scheme for the HE-NHP model is formed by these wave strengths

$$\begin{aligned} \widetilde{\alpha}_1 &= \tfrac{1}{2\tilde{c}^2}[(\widetilde{c} - \widetilde{u})\delta h + \delta q_u] \\ \widetilde{\alpha}_2 &= \tfrac{1}{2\tilde{c}^2}[(\widetilde{c} + \widetilde{u})\delta h - \delta q_u] \end{aligned} \tag{B.33}$$

and these source term values

$$\begin{aligned} \widetilde{\beta}_1 &= \tfrac{1}{2\tilde{c}^2}\left(g\widetilde{h}\delta z_b\right) \\ \widetilde{\beta}_2 &= -\widetilde{\beta}_1 \end{aligned} \tag{B.34}$$

B3.2. Strengths of the HR-NHP system

The four-wave numerical scheme for the HR-NHP model is formed by these wave strengths

$$\begin{aligned} \tilde{\alpha}_1 &= \tfrac{1}{2C_e^2}\left[-C_e\delta q_u + \delta h\left(\tilde{u}C_e + \tilde{c}^2\right) + \delta q_p\right] \\ \tilde{\alpha}_2 &= \tfrac{1}{2C_e^2}\left[C_e\delta q_u - \delta h\left(\tilde{u}C_e - \tilde{c}^2\right) + \delta q_p\right] \\ \tilde{\alpha}_3 &= \tfrac{1}{C_e^2}\left[\delta h\left(\tilde{p}_{nh} + k^2\right) - \delta q_p\right] \\ \tilde{\alpha}_4 &= \tfrac{1}{C_e^2}\left[C_e^2\delta q_w - \delta h\tilde{c}^2\tilde{w} - \tilde{w}\delta q_p\right] \end{aligned} \tag{B.35}$$

and these source term values

$$\begin{aligned} \tilde{\beta}_1 &= \tfrac{1}{2C_e^2}\left[C_e\left(\tilde{c}^2 - 2\tilde{p}_{nh}\right) + 2k^2\tilde{u}\right]\delta z_b \\ \tilde{\beta}_2 &= \tfrac{1}{2C_e^2}\left[-C_e\left(\tilde{c}^2 + 2\tilde{p}_{nh}\right) + 2k^2\tilde{u}\right]\delta z_b \\ \tilde{\beta}_3 &= -\tfrac{1}{C_e^2}\left(2k^2\tilde{u}\right)\delta z_b \\ \tilde{\beta}_4 &= -\tfrac{1}{C_e^2}\left(2k^2\tilde{u}\tilde{w}\right)\delta z_b \end{aligned} \tag{B.36}$$

B4. Well balance of numerical schemes

The well-balance schemes are those able to maintain the *lake at rest* condition. This is, the equilibrium [54,55]. In this section let us consider a quiescent surface over an arbitrary topography. A theoretical analysis of terms and equations is done for both considered models in this work in order to ensure well-balancing.

B4.1. HE-NHP system

The lake at rest initial condition implies null velocity ($hu = 0$ and $hw = 0$) and constant level ($\delta(h + z_b) = 0$). Additionally, with a static flow, the non-hydrostatic pressure is also null ($p_{nh} = 0$). In these conditions, numerical contributions at a generic cell edge, k, must be zero leading to

$$\left(\tilde{\tilde{\lambda}}^{\pm}\,\tilde{\tilde{\gamma}}\,\tilde{\tilde{\mathbf{e}}}_1\right)_k^m = 0 \quad \rightarrow \quad \left(\left(\tilde{\tilde{\lambda}}^{\pm}\,\tilde{\tilde{\alpha}} - \tilde{\tilde{\beta}}\right)\tilde{\tilde{\mathbf{e}}}_1\right)_k^m = 0 \tag{B.37}$$

being $m \in [1, 2]$ the waves, the final condition writes:

$$\left(\tilde{\lambda}^{\pm}\tilde{\alpha}\right)_k^m = \tilde{\beta}_k^m \tag{B.38}$$

In this model, as the first stage of the fractional step procedure is exactly the same as those of a SW model, the approach to ensure equilibrium is the same. Each of the 2 waves (λ_1 and λ_2) are analysed separately.

For wave 1, Eq. (B.38) leads to

$$(\tilde{u} - \tilde{c})\left(\frac{1}{2\tilde{c}^2}[(\tilde{c} - \tilde{u})\delta h + \delta q_u]\right) = \frac{1}{2\tilde{c}^2}\left(g\tilde{h}\delta z_b\right) \tag{B.39}$$

which applying initial conditions of rest ($u = 0$ and, thus, $q_u = 0$) and cancelling equal terms at both sides of equations yields

$$\delta h = \delta z_b \quad \rightarrow \quad \delta(h + z_b) = 0 \tag{B.40}$$

For wave 2 the same procedure is applied leading to

$$(\tilde{u} + \tilde{c})\left(\frac{1}{2\tilde{c}^2}[(\tilde{c} + \tilde{u})\delta h - \delta q_u]\right) = -\frac{1}{2\tilde{c}^2}\left(g\tilde{h}\delta z_b\right) \tag{B.41}$$

By applying the same conditions and cancelling terms, the equation provides the same condition as in wave 1, the rest condition with constant level (Eq. (B.40)).

The important issue in this model is to ensure that the pressure correction algorithm does not introduce any perturbation if the initial condition is the lake-at-rest condition (with w and p_{nh} null). For that purpose, the second algorithm of the fractional step procedure is now analysed.

Given an intermediate state computed from rest condition (fulfilling Eq. (B.38)), the non-hydrostatic pressure is computed as

$$(\mathcal{TH})\mathbf{P}_{nh}^{n+1} = \mathbf{D} \tag{B.42}$$

where TH stands for the matrix that contains the components A, B and C of the Poisson Eq. (47), $\mathbf{D}$ is the vector with the right hand side of the same equation (component D) and $\mathbf{P}_{nh}^{n+1}$ is the vector of the new unknown p_{nh}^{n+1} for each cell edge.

Following Eq. (B.1), no matter the value of A, B or C is, that D is null in rest conditions and, thus, the pressure vector must be null. Therefore, the lake-at-rest condition would remain constant in this model.

B4.2. HR-NHP system

The procedure to asses the C-property and the conservation of rest conditions in the HR-NHP model is the same as in the SW system, since in this case everything is integrated in the numerical contributions in cell edges, except the source term $\mathbf{S}_{nh}$, which is null in a static condition ($w = 0$ and $p_{nh} = 0$).

Therefore, the condition to fulfill with each wave in rest conditions is again

$$\left(\tilde{\lambda}^{\pm}\tilde{\alpha}\right)_k^m = \tilde{\beta}_k^m \tag{B.43}$$

where $m \in [1, 4]$ now considers the 4 waves of the system, that will be now assessed independently.

For wave 1, Eq. (B.43) leads to

$$(\tilde{u} - C_e)\left(\frac{1}{2C_e^2}\left[-C_e\delta q_u + \delta h\left(\tilde{u}C_e + \tilde{c}^2\right) + \delta q_p\right]\right) = \frac{1}{2C_e^2}\left[C_e\left(\tilde{c}^2 - 2\tilde{p}_{nh}\right) + 2k^2\tilde{u}\right]\delta z_b \tag{B.44}$$

that applying the rest condition leads to

$$-C_e\left(\delta h\tilde{c}^2\right) = \tilde{c}^2 C_e \delta h \tag{B.45}$$

which finally leads to the same condition as that in the SW model: $\delta h = -\delta z_b$. This is: $\delta(h + z_b) = 0$.

In wave 2, the approach is analogous leading to

$$(\tilde{u}+C_e)\left(\frac{1}{2C_e^2}\left[C_e\delta q_u-\delta h\left(\tilde{u}C_e-\tilde{c}^2\right)+\delta q_p\right]\right)=\frac{1}{2C_e^2}\left[-C_e\left(\tilde{c}^2+2\tilde{p}_{nh}\right)+2k^2\tilde{u}\right]\delta z_b \tag{B.46}$$

which provides the same equilibrium condition as wave 1.

For wave 3, the eigenvalue is directly $\tilde{u}$, therefore, although (B.43) leads to

$$\tilde{u}\left(\frac{1}{C_e^2}\left[\delta h\left(\tilde{p}_{nh}+k^2\right)-\delta q_p\right]\right)=-\frac{1}{C_e^2}\left(2k^2\tilde{u}\right)\delta z_b \tag{B.47}$$

everything gets cancelled ($0=0$) due to the multiplication by $\tilde{u}$ at both sides.

And, finally, the same happens with wave 4, where Eq. (B.43) writes

$$\tilde{u}\left(\frac{1}{C_e^2}\left[C_e^2\delta q_w-\delta h\tilde{c}^2\tilde{w}-\tilde{w}\delta q_p\right]\right)=-\frac{1}{C_e^2}\left(2k^2\tilde{u}\tilde{w}\right)\delta z_b \tag{B.48}$$

but the rest condition provides $0=0$.

References

[1] J.-P. Benque, A. Hauguel, P.-L. Viollet, Engineering Applications of Computational Hydraulics, vol. II, Pitman Books Limited, London, 1982.
[2] C. Ai, S. Jin, B. Lv, A new fully non-hydrostatic 3D free surface flow model for water wave motions, Int. J. Numer. Methods Fluids 66 (2011) 1354–1370.
[3] S. Kang, F. Sotiropoulos, Numerical modeling of 3D turbulent free surface flow in natural waterways, Adv. Water Resour. 40 (2012) 23–36.
[4] M. G, F. Shi, J.T. Kirby, Shock-capturing non-hydrostatic model for fully dispersive surface wave processes, Adv. Water Resour. 43–44 (2012) 22–35.
[5] V. Casulli, G.S. Stelling, Numerical simulations of 3D quasi-hydrostatic free-surface flows, J. Hydraul. Eng. 124 (1998) 678–686.
[6] W. Zhang, M. Uh Zapata, D.P. Van Bang, K.D. Nguyen, Three-dimensional hydrostatic curved channel flow simulations using non-staggered triangular grids, Water 14 (2022) 174.
[7] C.B. Vreugdenhil, Numerical Methods for Shallow-Water Flow, Kluwer Academic Publishers, Dordrecht, The Netherlands, 1994.
[8] O. Castro-Orgaz, H. Chanson, Undular and broken surges in dam-break flows: a review of wave breaking strategies in a Boussinesq-type framework, Environ. Fluid Mech. 20 (2020) 1383–1416.
[9] B.T. Nadiga, L.G. Margolin, P.K. Smolarkiewicz, Different approximations of shallow fluid flow over an obstacle, Phys. Fluids 8 (1995) 2066.
[10] C. Escalante, T. Morales de Luna, A general non-hydrostatic hyperbolic formulation for Boussinesq dispersive shallow flows and its numerical approximation, HAL Arch. Ouvert. (2020). (hal-02401138v2)
[11] N. Favrie, S. Gavrilyuk, A rapid numerical method for solving Serre–Green–Naghdi equations describing long free surface gravity waves, Nonlinearity (2017). IOP Publishing (hal-01358630v2)
[12] J.-L. Guermond, B. Popov, E. Tovar, C. Kees, Robust explicit relaxation technique for solving the Green–Naghdi equations, J. Comput. Phys. 399 (2019) 108917.
[13] S. Busto, M. Dumbser, C. Escalante, N. Favrie, S. Gavrilyuk, On high order ADER discontinuous Galerkin schemes for first order hyperbolic reformulations of nonlinear dispersive systems, J. Sci. Comput. 87 (2) (2021) 1–47.
[14] C. Bassi, L. Bonaventura, S. Busto, M. Dumbser, A hyperbolic reformulation of the Serre–Green–Naghdi model for general bottom topographies, Comput. Fluids 212 (2020) 104716.
[15] D.H. Peregrine, Long waves on a beach, J. Fluid Mech. 27 (1967) 815–827.
[16] P.A. Madsen, R. Murray, O.R. Srensen, A new form of the Boussinesq equations with improved linear dispersion characteristics. Part 1, Coastal Eng. 15 (1991) 371–388.
[17] P.A. Madsen, O.R. Srensen, A new form of the Boussinesq equations with improved linear dispersion characteristics. Part 2: a slowly varying bathymetry, Coastal Eng. 18 (1992) 183–204.
[18] F.N. Cantero-Chinchilla, R.J. Bergillos, P. Gamero, O. Castro-Orgaz, L. Cea, W.H. Hager, Vertically averaged and moment equations for dam-break wave modeling: shallow water hypotheses, Water 12 (11) (2020) 3232.
[19] E. Fernández-Nieto, M. Parisot, Y. Penel, J. Sainte-Marie, A hierarchy of dispersive layer-averaged approximations of euler equations for free surface flows, Commun. Math. Sci 16 (5) (2018) 1169–1202.
[20] C. Escalante, E.D. Fernández-Nieto, J. Garres-Díaz, T. Morales de Luna, Y. Penel, Non-hydrostatic layer-averaged euler system with layerwise linear horizontal velocity, HAL Arch. Ouvert. (2022). (hal-03676202)
[21] M.-O. Bristeau, A. Mangeney, J. Sainte-Marie, N. Seguin, An energy-consistent depth-averaged euler system: derivation and properties, Discrete Contin. Dyn. Syst. - B 20 (4) (2015) 961–988.
[22] J.D. Anderson Jr., Computational Fluid Dynamics: The Basics with Applications, Series in Mechanical Engineering, McGraw-Hill, USA, 1995.
[23] C. Hirsch, Numerical Computation of Internal and External Flows: The Fundamentals of Computational Fluid Dynamics, second ed., Butterworth-Heinemann, Oxford, 2007.
[24] Y. Yamazaki, Z. Kowalik, K. Fai Cheung, Depth-integrated, non-hydrostatic model for wave breaking and run-up, Int. J. Numer. Methods Fluids 61 (2009) 473–497.
[25] V. Casulli, A semi-implicit finite difference method for non-hydrostatic, free-surface flows, Int. J. Numer. Mehtods Fluids 30 (1999) 425–440.
[26] V. Casulli, A semi-implicit numerical method for the free-surface Navier–Stokes equations, Int. J. Numer. Mehtods Fluids 74 (2014) 605–622.
[27] N. Aissiouene, M.O. Bristeau, E. Godlewski, J. Sainte-Marie, A robust and stable numerical scheme for a depth-averaged euler system, HAL Open Sci. (2015). (hal-01162109v3f)
[28] C. Escalante, T. Morales de Luna, M.J. Castro, Non-hydrostatic pressure shallow flows: GPUimplementation using finite volume and finite difference scheme, Appl. Math. Comput. 338 (2018) 631–659.
[29] J. Burguete, P. Garcia-Navarro, Implicit schemes with large time step for non-linear equations: application to river flow hydraulics, Int. J. Numer. Methods Fluids 46 (6) (2004) 607–636.
[30] J. Fernández-Pato, M. Morales-Hernández, P. García-Navarro, Implicit finite volume simulation of 2D shallow water flows in flexible meshes, Comput. Methods Appl. Mech. Eng. 328 (2018) 1–25.
[31] M. Zijlema, Computation of free surface waves in coastal waters with swash on unstructured grids, Comput. Fluids 213 (2020) 104751.
[32] C. Escalante, M. Dumbser, M.J. Castro, An efficient hyperbolic relaxation system for dispersive non-hydrostatic water waves and its solution with high order discontinuous Galerkin schemes, J. Comput. Phys. 394 (2019) 385–416.
[33] A.J. Chorin, A numerical method for solving incompressible viscous flow problems, J. Comput. Phys. 2 (1) (1967) 12–26.
[34] G.S. Stelling, M. Zijlema, An accurate and efficient finite-difference algorithm for non-hydrostatic free-surface flow with application to wave propagation, Int. J. Numer. Methods Fluids 43 (2003) 1–23.

[35] I. Echeverribar, M. Morales-Hernndez, P. Brufau, P. Garcia-Navarro, 2D numerical simulation of unsteady flows for large scale floods prediction in real time, Adv. Water. Resour. 134 (2019) 103444.
[36] P. García-Navarro, J. Murillo, J. Fernández-Pato, I. Echeverribar, M. Morales-Hernández, The shallow water equations and their application to realistic cases, Environ. Fluid Mech. 19 (2019) 1235–1252.
[37] R. Hu, F. Fand, P. Salinas, C.C. Pain, N.D. Sto. Domingo, O. Mark, Numerical simulation of floods from multiple sources using an adaptive anisotropic unstructured mesh method, Adv. Water Resour. 123 (2019) 173–188.
[38] R. Vacondio, F. Aureli, F. Ferrari, P. Mignosa, A. Dal Pal, Simulation of the january 2014 flood on the Secchia River using a fast and high-resolution 2D parallel shallow-water numerical scheme, Nat. Haz. 80 (2016) 103–125.
[39] S.F. Bradford, B.F. Sanders, Finite-volume model for shallow-water flooding of arbitrary topography, J. Hydraul. Eng. 128 (3) (2002) 289–298.
[40] J. Murillo, P. García-Navarro, Weak solutions for partial differential equations with source terms: application to the shallow water equations, J. Comput. Phys. 229 (0) (2010) 4237–4368.
[41] J. Murillo, P. García-Navarro, Wave Riemann description of friction terms in unsteady shallow flows: application to water and mud/debris floods, J. Comput. Phys. 231 (2012) 1963–2001.
[42] J. Murillo, P. Garcia-Navarro, J. Burguete, P. Brufau, The influence of source terms on stability, accuracy and conservation in two-dimensional shallow flow simulation using triangular finite volumes, Int. J. Numer. Methods Fluids 54 (5) (2007) 543–590.
[43] J. Murillo, P. Garcia-Navarro, Accurate numerical modeling of 1D flow in channels with arbitrary shape. application of the energy balanced property, J. Comput. Phys. 260 (2014) 222–248.
[44] M.S. Ghidaoui, M. Zhao, D.A. McInnis, D.H. Axworthy, A review of water hammer theory and practice, Appl. Mech. Rev. 58 (2005) 49–76.
[45] P.K. Kundu, I.M. Cohen, Fluid Mechanics, Academic Press, Elsevier Science, San Diego (CA) (USA), 2001.
[46] R.K. Bullough, The wave par excellence, the solitary progressive great wave of equilibrium of the fluid: an early history of the solitary wave, in: Solitons, Springer Series, 1988, pp. 7–44.
[47] E.F. Toro, Riemann Solvers and Numerical Methods for Fluid Dynamics, Springer, Berlin, 1997.
[48] D. Baldwin, U. Gotkas, W. Hereman, L. Hong, R.A. Marino, J.C. Miller, Symbolic computation of exact solutions expressible in hyperbolic and elliptic functions for nonlinear PDEs, J. Symb. Comput. 37 (6) (2004) 669–705.
[49] M. Tonelli, M. Petti, Hybrid finite volume - finite difference scheme for 2DH improved Boussinesq equations, Coastal Eng. 56 (5–6) (2009) 609–620.
[50] C. Escalante, E.D. Fernández-Nieto, T. Morales de Luna, Y. Penel, J. Sante-Marie, Numerical simulations of a dispersive model approximating free-surface euler equations, J. Sci. Comput. 89 (55) (2021).
[51] A. Beji, J.A. Battjes, Experimental investigation of wave propagation over a bar, Coastal Eng. 19 (1993) 151–162.
[52] A. Beji, J.A. Battjes, Numerical simulation of nonlinear wave propagation over a bar, Coastal Eng. 23 (1994) 1–16.
[53] R. LeVeque, Numerical Methods for Conservation Laws, Lectures in Mathematics, ETH Zurich, Birkhuser Basel, 1992.
[54] A. Bermudez, M.E. Vazquez, Upwind methods for hyperbolic conservation laws with source terms, Comput. Fluids 23 (8) (1994) 1049–1071.
[55] A. Navas-Montilla, J. Murillo, 2D well-balanced augmented ADER schemes for the shallow water equations with bed elevation and extension to the rotating frame, J. Comput. Phys. 372 (2018) 316–348.